J. Fluid Mech. (2000), *vol.* 425, *pp.* 79–110. Printed in the United Kingdom

Boundary layer flow of air past solid surfaces in the presence of rainfall

By DIMITRIS N. SMYRNAIOS, NIKOLAOS A. PELEKASIS AND JOHN A. TSAMOPOULOS

Laboratory of Computational Fluid Dynamics, Department of Chemical Engineering, University of Patras, Patras 26500, Greece
e-mail: smyrnaios@chemeng.upatras.gr; pel@chemeng.upatras.gr; tsamo@chemeng.upatras.gr

(Received 4 November 1999 and in revised form 26 June 2000)

The steady two-dimensional laminar flow of an air stream, flowing past a solid surface at high Reynolds number, is examined in the presence of rainfall. As raindrops sediment on the surface they coalesce and form a continuous water film that flows due to shear, pressure drop and gravity, in general. In the limit as the boundary layer and film thickness remain smaller than the radius of curvature of the surface a simplified lubrication-type formulation describes the flow field in the film, whereas the usual boundary layer formulation is applied in the gas phase. In the case of a flat plate and close to the leading edge, $x \to 0$, a piecewise-self-similar solution is obtained, according to which creeping flow conditions prevail in the film and its thickness grows like $x^{3/4}$, whereas the Blasius solution is recovered in the air stream. Numerical solution of the governing equations in the two phases and for the entire range of distances from the leading edge, $x = O(1)$, shows that the film thickness increases as the rainfall rate, $\dot{r}$, increases or as the free-stream velocity, U_∞, decreases and that the region of validity of the asymptotic result covers a wide range of the relevant problem parameters. In the case of flow past a NACA-0008 airfoil at zero angle of attack a Goldstein singularity may appear far downstream on the airfoil surface due to adverse pressure gradients, indicating flow reversal and eddy formation inside the liquid film, and, possibly, flow separation. However, when the effect of gravity becomes evident in the film flow, as the Froude number decreases, and provided gravity acts in such a way as to negate the effect of the adverse pressure gradient, the location of the singularity is displaced towards the trailing edge of the airfoil and the flow pattern resembles that for flow past a flat plate. The opposite happens when gravity is aligned with the adverse pressure gradient. In addition it was found that there exists a critical water film thickness beyond which the film has a lubricating effect delaying the appearance of the singularity. Below this threshold the presence of the liquid film actually enhances the formation of the singularity.

1. Introduction

Dynamic interaction between a thin liquid film that grows on a solid surface and a gaseous boundary layer that surrounds the film and drives it to motion plays a key role (Campbell & Bezos 1989) in the performance loss that is often observed (Bezos *et al.* 1992) in wind tunnel tests of commercial airfoils under simulated rainfall conditions. In fact, intense rainfall and high wind shear are believed to

have caused a number of aircraft accidents that occurred under adverse weather conditions. Experimental investigations conducted at the NASA-Langley Low-Speed Wind-Tunnel facility (Hastings & Manuel 1985; Feo & Gonzalez 1988) captured the evolution of a continuous film as well as the formation of longitudinal waves on its interface, on either side of a NACA 64-210 airfoil under varying simulated rainfall conditions. Measurements on the upper airfoil surface for small angles of attack revealed a trend towards larger film thickness with increasing rainfall rate, $\dot{r}$, and decreasing Reynolds number, Re. In addition the film thickness invariably exhibited a maximum in the vicinity of the position of maximum airfoil thickness followed by a reduction in magnitude until, eventually, its continuity was disrupted halfway along the airfoil due to the formation of rivulets that evolved in the spanwise direction. It should be noted that film thickness as high as twice the local boundary layer thickness was measured, near the $x'/c = 0.3$ location, in this set of experiments; c is the chord length and x' denotes distance from the leading edge along the chord. As a result the above researchers were lead to the conjecture that the water film on the upper airfoil surface may be responsible for premature boundary layer separation, which also explains the reduction in the lift coefficient that is often observed under rainfall conditions.

As will be seen in the following sections such a flow pattern cannot be predicted by steady calculations only and the dynamic behaviour of the gas boundary layer/liquid film system has to be considered before a definite mechanism can be identified. However, a reliable base flow is essential for stability analysis to capture the actual transient response of the system. Previous studies focusing on the stability of two-phase flow at high Re (Hooper & Boyd 1987; Yih 1990) prescribe a piecewise linear velocity profile or a linear profile inside the film and a Blasius profile in the gas phase, while assuming rather than finding the location of the interface, thus failing to capture the evolution of film thickness in x in the base flow. This was remedied in a recent study by Nelson, Alving & Joseph (1995), where the asymptotic solution of the two-fluid boundary layer over a flat plate was obtained as the dimensionless distance from the leading edge increases, $\xi \to \infty$, for constant volume flow rate Q of the water layer; $\xi = \left(x'/\left(2\nu/U_\infty\right)\right)^{1/2}$ is scaled via the viscous penetration depth $2\nu/U_\infty$ where U_∞ denotes the free-stream velocity and ν the kinematic viscosity of air. In this context they found that the gas–liquid interface grows like $x'^{1/4}$ when the boundary layer in the air grows like $x'^{1/2}$, as part of a coupled self-similar solution according to which, as $x' \to \infty$, both water and air satisfy the Blasius boundary layer equations with a linear profile in the water and the flat-plate Blasius profile in the air. In other words, asymptotically, creeping flow conditions prevail in the film. This velocity profile, albeit without accounting for the predicted x-dependence of the base flow, has been used as the basis for a stability analysis by Timoshin (1997) in his study on high-Re instabilities in film-coated flows and by Ozgen, Degrez & Sarma (1998) in their study on the effect of de/anti-icing fluids on boundary layer stability.

Assuming simple shear in the water film amounts to neglecting film inertia in obtaining the base flow configuration. This may prove to be an important factor in the determination of the stability characteristics of the air–water system. In a different context, namely that of buoyancy-driven convection flow in settling vessels with inclined walls, it was shown by Shaqfeh & Acrivos (1987) that accounting for flow configuration inside the film of clear fluid that is generated on the downward facing surface of a settler can have a significant effect on the stability of the two-fluid system. This inertia is created as a result of the density difference between the clear fluid and the solid particles that are suspended in the liquid mixture contained in the settler.

The above researchers were able to do that by extending a base flow configuration previously obtained by Acrivos & Herbolzheimer (1979) which only accounted for the balance between buoyancy and shear in the clear fluid film. Shaqfeh & Acrivos (1986) extended the above base flow to account for film inertia, thus obtaining an improved structure that reduced to the one presented by Acrivos & Herbolzheimer in the limit as $x' \to 0; x'$ in this case denotes distance from the location on the plate where formation of the clear fluid layer is initiated. Stimulated by these findings and by the fact that, under intense rainfall, the water film inertia might become important, we have developed a model that accounts for the constant entrainment of water droplets in the film as well as film inertia.

The airstream is assumed to carry with it raindrops at a concentration too low, even for very large rainfall rates, to affect its dynamics. Even though raindrops can be as large as several mm in diameter, for the purposes of our study and following experimental investigations with water spray systems that produced clouds of droplets with mean droplet size as small as 20 μm (Thompson, Jang & Dion 1995), we take the drop size to be small so that the inertia of the droplets is negligible. It can be easily seen that for such small particle sizes the particles' Reynolds number, as defined via the Stokes velocity or via the shear due to the boundary layer, is very small. In addition, the shape of the raindrops is assumed to be nearly spherical since surface tension forces will not allow significant shape perturbations for such small particle size. As the rain particles sediment due to gravity they reach the airfoil, at a certain rainfall rate $\dot{r}$, where they coalesce and form a liquid film that flows under the action of shear from the gas stream. This flow pattern of shear-driven flow of a layer that is formed due to sedimentation of particles carried by a surrounding stream resembles the flow situation studied by Pelekasis & Acrivos (1995) in the context of convection and sedimentation of solid particles past a flat plate. Of course in the latter study solid particles do not coalesce. Rather they form a diffusion layer where their concentration increases from that in the free stream to their value on the plate as a result of the interplay between sedimentation and shear-induced resuspension. Nevertheless, certain similarities do exist between the two problems. Most notably, the combination of the shear stress balance and the mass balance at the interface between the gas stream and the concentrated particle layer (water film in the present study) gives rise to a similarity solution that describes the evolution of the particle layer near the leading edge of the plate. As will be seen in the next section this is possible in the context of the present study as well. The flow is taken to be laminar despite the fact that most modern wing sections are designed for very large Reynolds numbers. At this stage this will not pose any serious problem since the loss in performance has been observed in laminar airfoils as well (Thompson *et al.* 1995). It should also be noted that, if needed, turbulent boundary layers may be examined by considering alternative mean velocity distributions (Benjamin 1958).

Proceeding along these lines the steady evolution of the liquid film, flowing mainly under the action of shear from the air stream, is captured until the point where a Goldstein singularity appears (Goldstein 1948). This type of singularity is normally associated with points of zero shear at a solid wall and usually indicates flow separation. However, this is not always the case. Boundary layer singularities, in general, indicate flow reversal and are considered to be eddy creation mechanisms (Bhaskaran & Rothmayer 1998) that may or may not lead to separation. Since proper identification of the point of separation in the context of two-phase flow is not within the scope of the present study, we will refer to points of zero shear arising on the airfoil surface as Goldstein singularities or as points of flow reversal. Nevertheless, the

existence of such points can be used as a rough measure of the facility by which the air stream flows past a solid surface in the presence of a growing film and extensive reference will be made to them, upon their appearance, in § 5 where our results are discussed. In fact, it will be seen that film growth may enhance flow reversal, and consequently impair the flow of the air stream, below a certain, critical value of the rainfall rate. Beyond this value the film acts as a lubricant delaying the appearance of the Goldstein singularity.

The interaction between a growing liquid film, flowing due to the action of shear from a surrounding gas stream, and the stream can also play an important role in the context of heat transfer when the operating fluid is in the form of saturated vapour that is force-convected through the void space of a heat exchanger (Beckett & Poots 1972). As a result of the heat transfer process a film of condensate is formed that flows due to shear and, possibly, gravity. The interaction between the condensate and the vapour stream can have a significant effect on the heat transfer coefficient of the process, while wave formation can lead to quite similar flow patterns to the ones described at the beginning of this section. The steady-state evolution and growth of the condensate film can be obtained in a fashion similar to the rainfall problem. The case for film condensation under mixed forced–free convection past a vertical flat plate has been presented by Shu & Wilks (1995).

In § 2 the problem formulation at steady state is presented for two-dimensional flow of a gas stream past a curved solid surface on which a water film is generated, due to rainfall, and flows under the action of shear, pressure drop and gravity, in general. The specific model of rainfall is given in § 2.1 and the governing equations of the problem are written in § 2.2, based on the assumption that the radius of curvature of the surface is much larger than the boundary layer thickness. The leading-order asymptotic solution for flow past a flat plate is presented in § 3.1.1 as $\varepsilon \to 0$ or $x \to 0$; ε characterizes the ratio of film to boundary layer thickness whereas, the x-coordinate signifies the dimensionless distance from the leading edge of the plate. Corrections to the leading-order solution are obtained in § 3.1.2 in increasing powers of x. In § 3.2.1 the limit $\varepsilon \to 0$ is investigated for flow past a general solid surface with large radius of curvature while in § 3.2.2 and § 3.2.3 certain aspects of the NACA-0008 airfoil, which is the one that is investigated here as an example, are presented and discussed. Next, in § 4 the numerical method of solution of the full equations valid for $x = O(1)$ for a general curved surface is given. In § 5 the results of numerical simulations for flow past a flat plate and past a NACA-0008 airfoil are presented in the context of a parametric study and the effects of rainfall rate, $\dot{r}$, and free-stream velocity, U_∞, are discussed. Finally, in § 6 conclusions are drawn regarding the present as well as future investigations on the problem of performance loss due to rainfall.

2. Problem formulation

We wish to examine the two-dimensional laminar flow of an air stream at high $Re \equiv U_\infty L/\nu$, under conditions of rainfall, characterized by a constant rainfall rate, $\dot{r}$, past a solid surface. As mentioned before, the rain particle concentration in the gas phase is assumed to be too low to affect its dynamics. Therefore, the gas phase is treated as a pure fluid. Zero angle of attack is assumed for simplicity. Thus, far from the surface the air velocity assumes its free-stream value, U_∞ parallel either to a flat plate or to the chord-line of an airfoil, and at angle $\pi/2 - \beta$ with respect to gravity; see the schematic diagram in figure 1. Parameter β is defined as the angle between the gravity vector and the line perpendicular to the chord line of the surface. It assumes

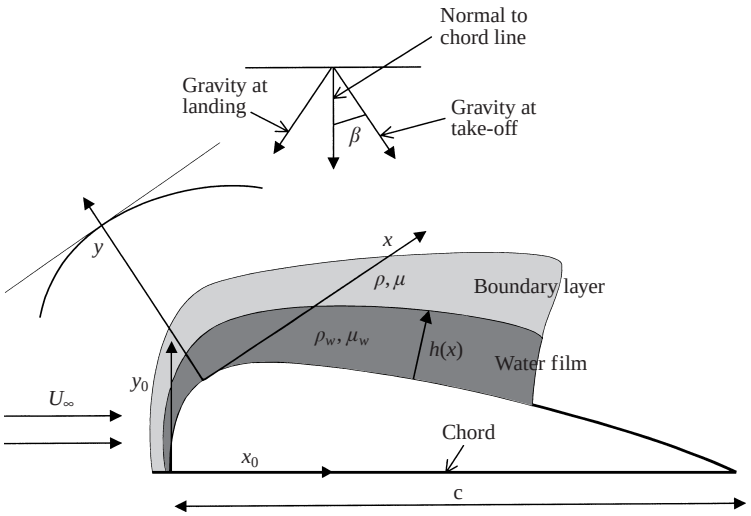

FIGURE 1. Schematic representation of the flow of a gas stream past an airfoil under conditions of rainfall.

positive (negative) values in order to simulate take-off (landing) of the plane. In order to simulate rainfall conditions, the air stream is assumed to be carrying along raindrops which, as they sediment on the plate, coalesce immediately and form a thin water film that covers the wing entirely and flows under the action of shear from the air stream. In reality there will be a small region near the leading edge of the wing where impact splashing takes place. Water ejecta from drop impacts interact with the boundary layer, while water drop cratering in the film generates an equivalent surface roughness, thus affecting the aerodynamic behaviour of the wing. We will neglect these two effects since, at the present stage of the analysis, we are interested in finding a quantitative relation between rainfall rate and interfacial wave formation and growth.

2.1. *Modelling of rainfall*

As a result of their small size the inertia of raindrops is very small, while their shape remains spherical due to surface tension. This allows their treatment in a fashion similar to that presented by Pelekasis & Acrivos (1995) in their study on sedimentation of solid particles that are convected past a flat plate. Thus, following the above investigators, the particle velocity in the air stream, $\boldsymbol{u}'_p$, is taken to be the sum of the local bulk velocity, $\boldsymbol{U}'$, and the particle slip velocity, $\boldsymbol{u}'_s$, with the primes indicating dimensional quantities:

$$\boldsymbol{u}'_p = \boldsymbol{U}' + \boldsymbol{u}'_s, \quad \boldsymbol{u}'_s = u_t f(\phi)\frac{\boldsymbol{g}}{g}, \tag{2.1}$$

where $\boldsymbol{g}$ is the gravitational acceleration, u_t is the Stokes terminal velocity, $f(\phi)$ is a hindrance function accounting for the influence of particle interactions; due to small particle size and concentration $f(\phi) \approx 1$. The first equality in (2.1) presupposes that the particle Reynolds number, whether in terms of the sedimentation velocity, or the local bulk shear rate, is vanishingly small,

$$Re_1 \equiv \frac{u_t a \rho}{\mu}, \quad Re_2 \equiv \left[\frac{U_\infty (L U_\infty / \nu)^{1/2}}{L}\right]\frac{a^2}{\nu}, \tag{2.2}$$

where ρ, μ, ν denote density, viscosity and kinematic viscosity of air, respectively, a is the characteristic radius of raindrops and L the characteristic length scale along the surface, normally the chord length of a model wing section. When $L \approx 30\,\text{cm}$, $U_\infty \approx 12\,\text{m s}^{-1}$ ($Re = 2.4\times10^5$), $a \approx 20\,\mu\text{m}$, the two dimensionless numbers in equation (2.2) become $Re_1 \approx 0.07$, $Re_2 \approx 0.5$.

The location of the air–water interface is determined by the mass balance of raindrops crossing the interface,

$$\boldsymbol{n}\cdot(\boldsymbol{U}' + \boldsymbol{u}'_s)\phi_s = \boldsymbol{u}'\cdot\boldsymbol{n}, \tag{2.3}$$

where $\boldsymbol{n}$ is the normal vector at the interface pointing towards the gas stream, ϕ_s is the particle volume fraction in the gas stream, and $\boldsymbol{u}'$ is the velocity at the interface and on the side of the film. In the following, variables in capital letters correspond to quantities defined in the gas phase, whereas variables in lower-case letters refer to the water film. Further manipulation of equation (2.3) gives

$$\phi_s u_t f(\phi_s)\boldsymbol{e}_g\cdot\boldsymbol{n} = \boldsymbol{u}'\cdot\boldsymbol{n} - \phi_s\boldsymbol{U}'\cdot\boldsymbol{n} \Rightarrow \phi_s u_t f(\phi_s)\boldsymbol{e}_g\cdot\boldsymbol{n} = u'_n(1-\phi_s), \tag{2.4}$$

where $\boldsymbol{e}_g$ is the unit vector in the direction of gravity. In the last equality use has been made on the fact that the bulk normal velocity is continuous at the interface ($\boldsymbol{U}' = \boldsymbol{u}'$). From previous studies (Dunham 1987), it has been established that the rainfall rate, $\dot{r}$, which is normally given by meteorological data for every geographical location, can be estimated through the rain particle concentration in the air and the terminal velocity as

$$\dot{r} = u_t f(\phi_s)\phi_s. \tag{2.5}$$

Consequently equation (2.4) becomes

$$\dot{r}\boldsymbol{e}_g\cdot\boldsymbol{n} = u'_n(1-\phi_s) \Rightarrow \dot{r}\boldsymbol{e}_g\cdot\boldsymbol{n} = u'_n. \tag{2.6}$$

The last equality is a result of the assumption that the particle volume fraction, ϕ_s, in the gas stream is very small. At this point it becomes evident that the difference between the present model and the one presented by Nelson *et al.* (1995) lies in the fact that in the latter a constant volumetric flow rate Q is prescribed for the film in the longitudinal direction, whereas here a constant drop influx, $\dot{r}$, is prescribed at every downstream position along the interface.

2.2. *Governing equations*

We now describe the flow inside the film and the boundary layer. To this end, we assume that the radius of curvature of the solid surface is much larger than the boundary layer or the film thickness. This is a commonly used assumption that is relevant to the flow situation considered here and simplifies the resulting equations significantly. As a result the flow domain is now described via a new set of coordinates, x, y, which are defined as distances measured along the solid surface and at right-angles to it, figure 1, so that they define a set of orthogonal curvilinear coordinates (Rosenhead 1963). Furthermore, assuming that all changes in physical quantities in the x-direction occur on a much larger length scale, L, than the film, H_f, and boundary layer, $LRe^{-1/2}$, thickness we can drop variations in the x-direction compared with variations normal to the solid surface (or the interface) as is normally done in boundary layer and lubrication theory; H_f is the characteristic film thickness, to be given a specific value later together with the characteristic film velocity, u_f, in the x-direction, and $LRe^{-1/2}$ is an estimate for the boundary layer thickness. In this context, and in terms of the curvilinear (x, y) coordinate system the flow description

in the gas phase assumes the familiar boundary layer form obtained for Cartesian coordinates, whereas lubrication-type equations govern the motion of the film.

Dependent variables characterizing the flow are non-dimensionalized using the following scaling quantities: $L, LRe^{-1/2}$, as characteristic length scales of the boundary layer type in the direction parallel to the solid surface, x, and perpendicular to it, Y, in the gas phase, respectively, U_∞, $U_\infty Re^{-1/2}$, as characteristic velocities along the x- and Y-directions in the gas phase, respectively, L, H_f, as characteristic length scales in the liquid film in the direction parallel to the solid surface, x, and perpendicular to it, y, respectively, $u_f, u_f H_f/L$, as characteristic velocities along the x- and y-directions in the liquid film, respectively and ρU_∞^2, as the inertial scale for pressure in both phases. It should be noted that gravity has been incorporated in the pressure term in both phases. This ensures that pressure in the gas phase approaches that obtained for standard potential flow in the limit $Y \to \infty$, while introducing a buoyancy-type term in the momentum equation of the film. In this context, and ignoring terms which are $O(Re^{-1/2}), O(H_f/L)$, or smaller, the governing equations become in the gas phase (in the following dependent variables pertaining to the gas phase are indicated by an upper case):

potential flow in the far field

$$Y \to \infty, \quad U \to U_p(x), \tag{2.7}$$

x-momentum

$$U\frac{\partial U}{\partial x} + V\frac{\partial U}{\partial Y} = -\frac{\mathrm{d}P}{\mathrm{d}x} + \frac{\partial^2 U}{\partial Y^2}, \tag{2.8}$$

Y-momentum

$$\frac{\partial P}{\partial Y} = 0, \tag{2.9}$$

continuity

$$\frac{\partial U}{\partial x} + \frac{\partial V}{\partial Y} = 0. \tag{2.10}$$

At the gas–liquid interface $Y = \varepsilon H(x)$, $y = H(x)$:

continuity of tangential and normal velocity

$$U = \varepsilon\frac{\mu}{\mu_w}u, \quad V = \varepsilon^2\frac{\mu}{\mu_w}v, \tag{2.11a,b}$$

continuity of tangential and normal stress

$$\frac{\mu}{\mu_w}\frac{H_f}{u_f}\frac{U_\infty}{LRe^{-1/2}}\frac{\partial U}{\partial Y} = \frac{\partial u}{\partial y}, \quad P = p, \tag{2.12a,b}$$

liquid mass balance upon evaluating (2.6) at the interface

$$\left(\cos\beta\frac{\partial y}{\partial y_0} - \sin\beta\frac{\partial y}{\partial x_0}\right) = \frac{u_f H_f}{\dot{r}L}\left(u\frac{\mathrm{d}H}{\mathrm{d}x} - v\right); \tag{2.13}$$

and in the water film (in the following dependent variables pertaining to the film are indicated by a lower case):

continuity

$$\frac{\partial u}{\partial x} + \frac{\partial v}{\partial y} = 0, \tag{2.14}$$

x-momentum

$$\varepsilon^2\frac{\rho_w}{\rho}\left(\frac{\mu}{\mu_w}\right)^2\left(u\frac{\partial u}{\partial x}+v\frac{\partial u}{\partial y}\right)=-\frac{\mathrm{d}p}{\mathrm{d}x}+\frac{1}{Fr}\left(\frac{\rho_w}{\rho}-1\right)\left(\sin\beta\frac{\partial x}{\partial x_0}-\cos\beta\frac{\partial x}{\partial y_0}\right)+\frac{1}{\varepsilon}\frac{\partial^2 u}{\partial y^2}, \tag{2.15}$$

y-momentum

$$\frac{\partial p}{\partial y}=\frac{gH_f}{U_\infty^2}\left(\frac{\rho_w}{\rho}-1\right)\left(\sin\beta\frac{\partial y}{\partial x_0}-\cos\beta\frac{\partial y}{\partial y_0}\right), \tag{2.16}$$

no-slip and no-penetration on the solid surface

$$u=v=0 \quad \text{at } y=0. \tag{2.17}$$

In the above $\varepsilon\equiv H_f/(LRe^{-1/2})$ is a measure of the ratio between the film and the boundary layer thickness, x_0, y_0, denote Cartesian coordinates defined in the direction of the oncoming flow and perpendicular to it (figure 1), respectively, scaled with L, $U_p(x)$ is the potential flow solution for flow around the solid surface, scaled with U_∞ and the subscript w signifies physical properties in the liquid film. It should also be noted that the direct boundary layer calculation is adopted here and the pressure drop inside the film is prescribed by flow conditions in the far field, as can also be surmised by the treatment of pressure variation inside the two phases. Owing to the large radius of curvature of the surface, partial derivatives of the curvilinear coordinates, x, y, with respect to x_0 and y_0 are evaluated at the solid surface and take the form

$$\frac{\partial x}{\partial x_0}=\frac{1}{\sqrt{1+(\mathrm{d}S/\mathrm{d}x_0)^2}}\left(1+O\left(\frac{H_f}{k}\right)z\right), \quad \frac{\partial x}{\partial y_0}=\frac{\mathrm{d}S/\mathrm{d}x_0}{\sqrt{1+(\mathrm{d}S/\mathrm{d}x_0)^2}}\left(1+O\left(\frac{H_f}{k}\right)z\right), \tag{2.18}$$

$$\frac{\partial y}{\partial x_0}=-\frac{\mathrm{d}S/\mathrm{d}x_0}{\sqrt{1+(\mathrm{d}S/\mathrm{d}x_0)^2}}, \quad \frac{\partial y}{\partial y_0}=\frac{1}{\sqrt{1+(\mathrm{d}S/\mathrm{d}x_0)^2}}, \tag{2.19}$$

where k is a measure of the surface radius of curvature and $y_0=S(x_0)$ denotes the shape of the solid surface, also scaled with L.

In order to balance terms in the tangential stress balance (2.12a), and the liquid mass balance, (2.13), we define, u_f and H_f such that

$$\frac{u_f}{\dot{r}}\frac{H_f}{L}=1, \quad \frac{u_f}{U_\infty}\frac{\mu_w}{\mu}=\frac{H_f}{LRe^{-1/2}}.$$

Thus, we obtain a measure for the film thickness, H_f, and the film velocity u_f,

$$\frac{H_f}{L}=Re^{-1/4}\left(\frac{\mu_w}{\mu}\right)^{1/2}\left(\frac{\dot{r}}{U_\infty}\right)^{1/2}, \tag{2.20}$$

$$\frac{u_f}{U_\infty}=Re^{1/4}\left(\frac{\mu}{\mu_w}\right)^{1/2}\left(\frac{\dot{r}}{U_\infty}\right)^{1/2}. \tag{2.21}$$

Consequently, the steady state of the air–water system can be calculated via solution of (2.7)–(2.17), given the following parameters of the problem: the air to water viscosity ratio, μ/μ_w, the air to water density ratio, ρ/ρ_w, the thickness ratio between the film and the boundary layer in the air stream, ε, the angle, β, between gravity and the negative y_0-direction of the solid surface, and the Froude number, $Fr\equiv U_\infty^2/(gL)$. The

effect of surface tension on the normal force balance, (2.12*b*), has been neglected and the effect of gravity on the pressure drop across the water film, (2.16), will be neglected owing to the small value of the inverse Weber number, $We^{-1} \equiv (\sigma/\rho U_\infty^2)(H_f/L^2)$, and the large value of the 'transverse' Froude number, $Fr_y = U_\infty^2/(gH_f) = FrL/H_f$. In particular, integration of the transverse pressure drop, (2.16), along the y-direction and application of the normal force balance, (2.12*b*), provides the pressure inside the film and consequently the longitudinal pressure drop as a function of that in the air:

$$\frac{\partial p}{\partial x} = \frac{\partial P}{\partial x} - \frac{gH_f}{U_\infty^2}\left(\frac{\rho_w}{\rho} - 1\right)\frac{\mathrm{d}}{\mathrm{d}x}\left[H(x)\left(\sin\beta\frac{\partial y}{\partial x_0} - \cos\beta\frac{\partial y}{\partial y_0}\right)\right].$$

Thus, the contribution due to the film thickness variation is $O(H_f/L)$ smaller than the gravitational one. Finally, as can be seen from the x-momentum equation (2.15) in the water film, the motion of the film is determined by the longitudinal pressure drop, $\mathrm{d}P/\mathrm{d}x$, which is imposed on it from the boundary layer in the gas stream, by shear forces, $(1/\varepsilon)(\partial^2 u/\partial y^2)$, whose relative magnitude increases with decreasing film thickness or decreasing ε, and gravity,

$$\frac{1}{Fr}\left(\frac{\rho_w}{\rho} - 1\right)\left(\sin\beta\frac{\partial x}{\partial x_0} - \cos\beta\frac{\partial x}{\partial y_0}\right),$$

whose magnitude is characterized by $1/Fr$, β, and ρ_w/ρ.

3. Asymptotic solution

3.1. *Flow past a flat plate*

As a first step towards understanding better the behaviour of the air–water system under conditions of rainfall, we study flow past a flat plate when gravity is at right-angles to the oncoming flow, $\beta = 0$. In this case $S(x_0) = 0$ while the Cartesian and curvilinear coordinate systems coincide. The motion of the film is due solely to the shear stress exerted upon it from the surrounding gas stream, whereas pressure drop and gravity vanish due to the geometry.

3.1.1. *Solution when* $\varepsilon = 0$, or $x = 0$

As can be easily seen from the set of equations given in the previous section, when the film thickness is much smaller than the boundary layer thickness, $\varepsilon \to 0$, the flow pattern in the gas phase is described by the usual Blasius equations, whereas creeping flow conditions exist in the water film with the shear rate remaining constant at each downstream location as prescribed by the Blasius solution at the interface. At the same time the thickness of the film is given by the particle mass balance. More specifically, the solution for the film flow becomes

$$H_0(x) = x^{3/4}\sqrt{\frac{2}{0.332}}, \quad u_0 = x^{1/4}\sqrt{0.664}\,\frac{y}{H_0(x)}, \quad v_0 = \frac{1}{2}\left(\frac{y}{H_0(x)}\right)^2, \tag{3.1}$$

with subscript zero indicating that this solution corresponds to the leading-order, $O(\varepsilon^0)$, term of an expansion in powers of ε. Clearly, then, this solution resembles the asymptotic result of Nelson *et al.* (1995) in that it neglects the effect of interia in the film while adopting the Blasius profile in the gas phase. The basic differences between the two lie in the growth rate of the film thickness, $x^{3/4}$ vs. $x^{1/4}$, and the fact that, as will be seen in the next section, inertia becomes important here as x increases.

3.1.2. *Higher-order corrections*

The parameter ε essentially defines a new length scale, L^*, for which the thickness of the two layers become comparable, i.e.

$$\varepsilon = \frac{H_f}{LRe^{-1/2}} = \frac{LRe^{-1/4}(\mu_w/\mu)^{1/2}(\dot{r}/U_\infty)^{1/2}}{LRe^{-1/2}} = 1.$$

Then, it can be shown that the asymptotic solution obtained in the previous section in the limit $\varepsilon \to 0$ can be recovered as the leading-order term, $O(x^0)$, of an expansion in rising powers of x, with $x \to 0$ signifying distances from the leading edge of the plate for which, $x' \ll L^*$. Indeed setting $\varepsilon = 1$ gives rise to the following set of equations in the gas phase:
free-stream condition

$$Y \to \infty, \quad U \to 1, \tag{3.2}$$

x-momentum

$$U\frac{\partial U}{\partial x} + V\frac{\partial U}{\partial Y} = \frac{\partial^2 U}{\partial Y^2}, \tag{3.3}$$

continuity

$$\frac{\partial U}{\partial x} + \frac{\partial V}{\partial Y} = 0; \tag{3.4}$$

on the film/air interface, $Y = y = H(x)$:
continuity of tangential and normal velocity

$$U = \frac{\mu}{\mu_w}u, \quad V = \frac{\mu}{\mu_w}v, \tag{3.5a,b}$$

continuity of tangential stress

$$\frac{\partial U}{\partial Y} = \frac{\partial u}{\partial y}, \tag{3.6}$$

particle mass balance

$$u\frac{\mathrm{d}H}{\mathrm{d}x} - v = 1; \tag{3.7}$$

and in the water film:

x-momentum

$$\frac{\rho_w}{\rho}\left(\frac{\mu}{\mu_w}\right)^2\left(u\frac{\partial u}{\partial x} + v\frac{\partial u}{\partial y}\right) = \frac{\partial^2 u}{\partial y^2}, \tag{3.8}$$

continuity

$$\frac{\partial u}{\partial x} + \frac{\partial v}{\partial y} = 0, \tag{3.9}$$

no-slip and no-penetration at the solid surface

$$u = v = 0 \quad \text{at } y = 0. \tag{3.10}$$

This set of equations admits a series solution for the boundary layer

$$U = \sum_{\kappa=0}^{\infty} x^{\kappa/4}F'_\kappa(\eta), \; V = \sum_{\kappa=0}^{\infty} x^{\kappa/4-1/2}\left(\frac{\eta F'_\kappa(\eta)}{2}\left(\frac{\kappa}{4} - \frac{1}{2}\right)F_\kappa(\eta)\right), \quad \eta \equiv \frac{Y}{x^{1/2}}, \tag{3.11}$$

for the location of the interface

$$H(x) = \sum_{\kappa=0}^{\infty} A_\kappa x^{(\kappa+3)/4}, \tag{3.12}$$

and for the water film

$$\left.\begin{aligned} u &= \sum_{\kappa=0}^{\infty} G'_\kappa(z) x^{(\kappa+1)/4}, \quad v = \sum_{\kappa=0}^{\infty} x^{\kappa/4} \sum_{j=0}^{\kappa} A_\kappa \left(z G'_{\kappa-j}(\eta) \frac{j+3}{4} - G_{\kappa-j}(\eta) \frac{\kappa+4}{4} \right), \\ z &\equiv \frac{y}{H(x)}. \end{aligned}\right\} \tag{3.13}$$

The leading-order terms in the above expansions satisfy the Blasius equation in the gas stream

$$2F_0''' + F_0'' F_0 = 0 \quad \text{with} \quad F'(\eta \to \infty) = 1 \quad \text{and} \quad F(\eta = 0) = F'(\eta = 0) = 0, \tag{3.14}$$

continuity of shear and mass balance at the interface

$$F_0''(\eta = 0) = \frac{G_0''(z=1)}{A_0}, \quad A_0 = \frac{1}{G_0(z=1)}, \tag{3.15}$$

whereas creeping flow prevails in the film

$$G_0'''(z) = 0, \tag{3.16a}$$

with the usual no-slip, no-penetration conditions at the solid surface

$$G_0(z=0) = G_0'(z=0) = 0. \tag{3.16b}$$

Thus, we obtain $G_0(z) = \sqrt{0.332/2}z^2$, $A_0 = \sqrt{2/0.332}$. This is the same solution as the one presented in § 3.1.1 when ε was set to 0. The first correction to the leading-order solution satisfies the following set of equations: in the gas phase

$$F_1'(\eta \to \infty) = 0, \quad F_1''' + \frac{F_1'' F_0}{2} - \frac{F_1' F_0'}{4} + \frac{3}{4} F_0'' F_1 = 0, \tag{3.17}$$

at the interface $\eta = 0$, $z = 1$

$$F_1 = 0 \quad F_1' = -A_0 F_0'' + \frac{\mu}{\mu_w} G_0', \tag{3.18a,b}$$

$$A_1 = -A_0 \frac{G_1}{G_0}, \quad G_1'' = A_0 F_1'' + A_0^2 F_0'''' + A_1 F_0'', \tag{3.18c,d}$$

and in the film,

$$G_1''' = 0 \quad \text{with} \quad G_1(z=0) = G_1'(z=0) = 0, \tag{3.19}$$

reflecting the effect of increased displacement thickness due to the film growth.

Using information from the leading-order solution, (3.17) and (3.18*a*, *b*) can be solved to give $F_1(\eta)$ leaving (3.18*c*, *d*) and (3.19) for calculating A_1 and $G_1(z)$. In fact, from (3.17) we obtain that $F^1 = c_0 F_0'$, where c_0 is a constant to be evaluated using (3.18*b*). Thus, (3.18*d*) gives $G_1''(z=1) = 0$, and consequently from (3.18*c*) $A_1 = 0$ and the $O(x)$ correction for the film thickness is zero. Figure 2 shows the evolution of the film thickness as predicted by the leading-order approximation and as calculated via numerical solution of (3.2)–(3.10) as discussed in § 4. Due to the vanishing first-order correction, the leading-order solution for the film thickness provides a reliable

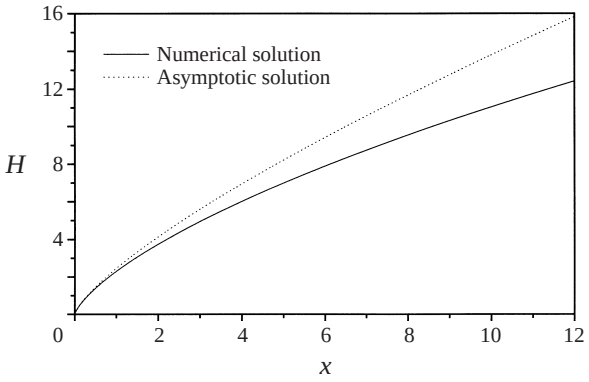

FIGURE 2. Evolution of the dimensionless film thickness H with increasing distance x from the leading edge as predicted by the zeroth order asymptotic solution, and as calculated by the numerical solution of the full equations.

prediction of the full problem even when $x = O(1)$. The deviation between the leading order, $O(x^{3/4})$, prediction for the film thickness and the numerical solution increases when $x \gg 1$, basically due to the effect of inertia as can be surmised from the fact that the creeping flow result over-predicts the film thickness. The delayed appearance of the effect of inertia can be explained by resorting to the series solution of the problem and noting that the left-hand side of (3.8) will first contribute to the series solution at third order, since $G_0'''(z) = G_1'''(z) = G_2'''(z) = 0$.

A similar series solution has been obtained by Beckett & Poots (1972) for flow past a flat plate at high Re in the presence of film condensation, albeit in the form of a power series in ε. It should be pointed out that the series expansion in powers of $x^{1/4}$, for fixed $\varepsilon = 1$, that was given above can also be viewed as an expansion in powers of $\varepsilon, \varepsilon \ll 1$, with x remaining $O(1)$ and scaled via L, which is treated as an additional problem parameter. For example the longitudinal velocity in the gas stream assumes the form $U = \sum_{\kappa=0}^{\infty} \varepsilon^{\kappa} x^{\kappa/4} F_{\kappa}'(\eta)$, and similarly for the rest of the unknowns. This type of solution, whether in terms of x or in terms of ε, represents an asymptotic series rather than a converging series; see also Bender & Orszag (1978). It is not uncommon that such asymptotic solutions in terms of a small parameter provide a reasonable approximation to the exact solution, sometimes, with increased overall validity compared to existing converging series.

Indeed, the leading-order solution constitutes a valid base flow for a wide range of the physical quantities that are relevant to our problem. For example, when a wing section of 70 cm length is placed parallel to an air stream with free-stream velocity $10\,\mathrm{m\,s^{-1}}$, and subjected to a moderate rainfall rate $\dot{r} = 100\,\mathrm{mm\,h^{-1}}$, which is a quite realistic set of parameters for wind tunnel testing, setting $\varepsilon = 1$ gives $L^* \approx 62\,\mathrm{m}$. Consequently, since $L/L^* \approx 0.01$, the entire wing lies in the region of validity of the zeroth-order solution. However, as the rainfall rate increases, L^* decreases significantly and a tenfold increase of $\dot{r}$ would yield $L^* \approx 0.6\,\mathrm{m}$, in which case film inertia starts playing an important role in the problem.

3.2. *Flow past a curved surface*

Unlike the case for flow past a flat plate, when a general curved surface is considered the solution in the two limits, $\varepsilon \to 0$ and $x \to 0$, does not behave in the same way. Keeping in mind that we are mostly interested in surfaces with a rounded leading

edge where the geometrical characteristics are distinctly different from the rest of the surface we expect that the limit $x \to 0$ will present certain difficulties in the analysis. In the following we discuss these issues and present the approach adopted in this study in order to circumvent them.

3.2.1. *Solution in the limit* $\varepsilon \to 0$

When ε is very small the thickness of the film is negligible compared with that of the boundary layer and the solution in the gas phase reduces to that obtained for dry conditions in the air stream flowing past the same curved surface. This decouples the solution in the gas phase which can now be solved independently to provide the shear stress, $f_1(x) \equiv (\partial U/\partial Y)(Y = 0)$, at the interface, see also Rosenhead (1963). It can be easily seen, by combining the definition of $\varepsilon = H_f/(LRe^{-1/2})$ with (2.11)–(2.17) and (2.20), (2.21), that the problem formulation in the liquid film becomes in this limit

$$f_1(x) = \frac{\partial u}{\partial y}, \quad f_3(x) = u\frac{\mathrm{d}H}{\mathrm{d}x} - v \quad \text{at } y = H(x), \tag{3.20}$$

$$\frac{\partial u}{\partial x} + \frac{\partial v}{\partial y} = 0, \tag{3.21}$$

$$\frac{\partial^2 u}{\partial y^2} = 0, \tag{3.22}$$

$$u = v = 0 \quad \text{at } y = 0, \tag{3.23}$$

where

$$f_1(x) \equiv \frac{\partial U}{\partial Y}(Y = 0), \quad f_3(x) \equiv \left(\cos\beta\frac{\partial y}{\partial y_0} - \sin\beta\frac{\partial y}{\partial x_0}\right)$$

are introduced for convenience.

Film flow now occurs solely due to shear from the surrounding boundary layer, while the velocity field and film thickness take the form

$$u = yf_1(x), \quad v = -\frac{y^2}{2}f_1'(x), \quad H(x) = \left(2\frac{\int_0^x f_3(x)\mathrm{d}x}{f_1(x)}\right)^{1/2}. \tag{3.24}$$

As $x \to 0$ the film thickness becomes $H(0) = (2\sin\beta/(\mathrm{d}f_1/\mathrm{d}x)(x = 0))^{1/2}$. As will be seen in the following, for the surface geometries considered here the flow near the leading edge resembles flow in the neighbourhood of the forward stagnation point of a cylinder due to the rounded shape of airfoils near the leading edge, in which case $(\mathrm{d}f_1/\mathrm{d}x)(x = 0) = 1.2325C^{3/2}$; $x \to 0$ $U_p \sim xC$, where $C > 0$ and is given in the next section (see also Rosenhead 1963). On the other hand, when the angle β is negative the prediction for the film thickness at the leading edge becomes unrealistic. At this point further discussion is needed on the characteristics of the solid surface, particularly near the leading edge, and the complications that may arise as a result of that.

In an attempt to obtain a first-order correction in ε to the above leading-order solution we note that, due to the small value of the viscosity ratio μ/μ_w for the air/water system, and as long as the film thickness remains relatively small, the film is, roughly, subjected to the shear stress $f_1(x)$, as this is provided by the solution for a dry airfoil even when ε is $O(1)$; see boundary condition (2.11*a*, *b*). In addition, as

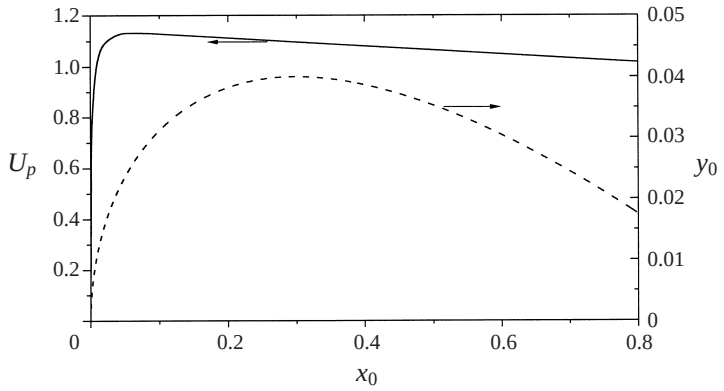

FIGURE 3. - - - -, Geometric shape of the NACA-0008 wing section; ——, tangential velocity on the surface of a NACA-0008 airfoil as predicted by potential theory.

will be seen in the following, pressure drop dominates gravity for most of the flow past an airfoil. As a result, longitudinal velocity satisfies, approximately, the following equation:

$$\frac{\partial^2 u}{\partial y^2} = \varepsilon \frac{\partial p}{\partial x}, \tag{3.25}$$

while the rest of the problem formulation remains the same as prescribed by (3.20), (3.21) and (3.23). Then the longitudinal velocity in the film, u, and its thickness, H, are given by

$$u = \varepsilon \frac{\mathrm{d}p}{\mathrm{d}x}\frac{y^2}{2} + \left(f_1 - \varepsilon H \frac{\mathrm{d}p}{\mathrm{d}x}\right) y, \quad \frac{\mathrm{d}H}{\mathrm{d}x} = \frac{f_3(x) - \frac{1}{2}H^2\,\mathrm{d}f_1/\mathrm{d}x + \varepsilon\frac{1}{3}H^3\,\mathrm{d}^2p/\mathrm{d}x^2}{Hf_1(x) - \varepsilon\,(\mathrm{d}p/\mathrm{d}x)\,H^2} \tag{3.26}$$

The last equation will be very useful in explaining the results presented in § 5.2 for the evolution of the film thickness with increasing ε for flow past a NACA-0008 airfoil.

3.2.2. *Characteristics of the NACA-0008 airfoil*

There are certain aspects of the treatment of the flow past a curved surface that warrant special discussion. The first concerns the potential flow solution for an airfoil. We chose to study flow at zero angle of attack past a NACA-0008 wing section, which is an airfoil with well-documented aerodynamic properties that has a simple thin symmetric shape, not dissimilar from that of a flat plate. Its maximum thickness is 8% of its chord length and near the leading edge its shape approaches that of a circle with radius of curvature, ρ_L, 0.7% of the chord length (Abbott & Doenhoff 1949). In order to obtain the potential flow solution for the velocity distribution along the airfoil surface, to be used as the far-field velocity for the boundary layer solution, we employed Theodorsen's theory, a brief description of which is given below.

This approach initially utilizes a series of transformations in order to map the original airfoil shape onto a circle. Then via the use of Poisson's integral equation (Thwaites 1960) the radius of the circle onto which the airfoil surface is mapped is obtained as well as the angular distance $\varphi(\theta)$, that relates the arguments of the airfoil's complex representation in the original and transformed domains, as a function of the polar angle θ. Finally, using the formula that gives the speed on the surface of a cylinder, in conjunction with the Kutta–Joukowski condition that guarantees finiteness of the velocity at the trailing edge, we obtain the velocity distribution on

the airfoil surface (Thwaites 1960). Figure 3 shows the shape and tangential velocity on the surface of the NACA-0008 airfoil as obtained by the above method. The solution compares well with tabulated values at certain downstream locations along the chord line which are available in the literature (Abbott & Doenhoff 1949). Its validity is questionable near the trailing edge only, but this does not affect our analysis since most of the dynamic phenomena that we are interested in capturing happen long before the film reaches the region near the trailing edge.

The asymptotic solution for flow past a cylinder will be utilized in order to start the time-like integration process in the x-direction for flow past a NACA-0008 airfoil. As mentioned before, the shape of this airfoil near the leading edge resembles a circular arc; in dimensional Cartesian coordinates $y_0' \propto \sqrt{2\rho_L}\sqrt{x_0'}$ as $x_0 \to 0$ with ρ_L denoting the leading-edge radius of curvature. Consequently, the velocity near the leading edge, as predicted by potential flow considerations, behaves like $U_p \propto 2xL/\rho_L = xC$ with $C = 285.7$ for the type of airfoil considered here, which is the asymptotic behaviour near the leading edge of the velocity distribution, $U_p = 2\sin\theta$ with $\theta = 0$ at the leading edge, for potential flow past a cylinder at zero angle of attack; L denotes the chord length of the airfoil that is used in order to scale distances x along its surface. Then the well-known asymptotic solution for boundary layer flow past a cylinder can be used, valid near the forward stagnation point, $x \to 0$, according to which the longitudinal velocity grows like x while the transversal velocity remains non-zero (Rosenhead 1963).

This is a very important aspect of the flow past a curved surface, especially when the effect of gravity is considered near the leading edge. In particular, for the two cases of interest to us, corresponding to the position assumed by an airfoil during landing or taking off, the angle β is such that the buoyancy force points towards the lower part of the airfoil surface. Since this is the only force that survives in the limit as $x \to 0$, for an airfoil with a rounded leading edge resembling a circular arc where pressure drop and shear vanish, it would tend to drive the film in the opposite direction. This seems to be another problem pertaining to the solution near the leading edge, besides the negative rain particle accumulation, $f_3(x = 0) < 0$, when $\beta < 0$. Despite all this it will be seen that such problems arise in such a narrow region near $x = 0$, for the parameter range of interest here, that they do not really constitute a serious drawback of the model. It is, anyway, well known that very close to the leading edge the problem formulation that was given in the previous section is not valid any more because $x' \approx \nu/U_\infty$. Moreover, the radius of curvature of the airfoil becomes much larger than the boundary layer thickness as x approaches zero.

Plotting f_3 as a function of x when β takes values in the interval $(-5^\circ, 5^\circ)$, which is quite adequate for the purposes of our study, we can see that it can only be negative when β is negative, and this only happens in a very narrow region near the leading edge ($0 \leqslant x \leqslant 0.001$), becoming positive beyond this range of values, figure 4(*a*). As far as the issue of the gravitational force pushing the film towards the lower airfoil surface is concerned, careful examination of the x momentum reveals that the negative pressure drop, $-\mathrm{d}p/\mathrm{d}x$, acquires huge values near the forward stagnation point, even though it is zero when $x = 0$, to the extent that it dominates gravitational forces for x values as small as 0.001. Figure 4(*b*) shows the evolution of

$$f_2(x) = -\frac{\mathrm{d}p}{\mathrm{d}x} + \left(\frac{\rho_w}{\rho} - 1\right)\frac{1}{Fr}\left(\sin\beta\frac{\partial x}{\partial x_0} - \cos\beta\frac{\partial x}{\partial y_0}\right)$$

and $-\mathrm{d}p/\mathrm{d}x$, when $\beta = 0^\circ$ and $Fr = 67$, one of the lower values for Fr used in this study, clearly demonstrating the dominance of the pressure term near $x = 0$, even

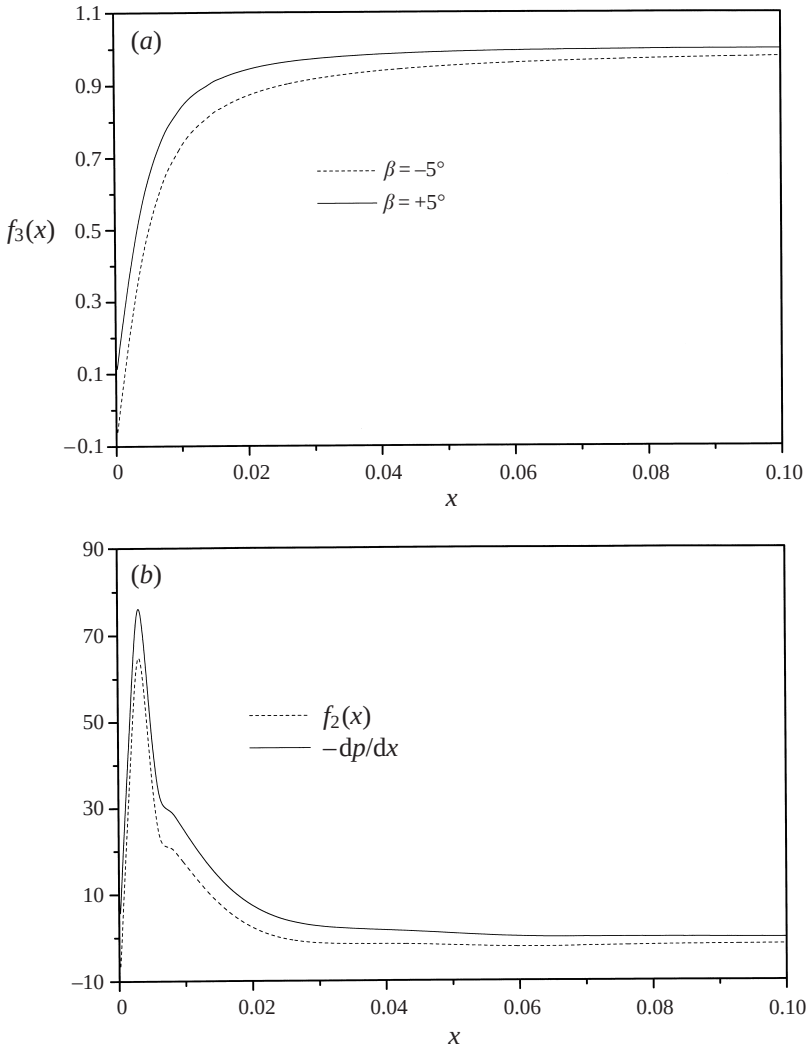

FIGURE 4. (*a*) Evolution of the function $f_3(x)$, indicating the rate by which raindrops enter the water film, for different values of angle β; (*b*) evolution of pressure drop, $-\mathrm{d}p/\mathrm{d}x$ and function $f_2(x)$, which contains both pressure drop and gravity.

though at $x = 0$ gravity is the only surviving force. This should be expected since

$$-\frac{\mathrm{d}p}{\mathrm{d}x} = U_p \frac{\mathrm{d}U_p}{\mathrm{d}x} \propto 4x \left(\frac{L}{\rho_L}\right)^2 = 81632x$$

for a NACA-0008 airfoil, whereas

$$\left(\frac{\rho_w}{\rho} - 1\right) \frac{1}{Fr} \left(\sin\beta \frac{\partial x}{\partial x_0} - \cos\beta \frac{\partial x}{\partial y_0}\right) \approx \frac{-1000\cos\beta}{50} \approx -20$$

near the leading edge. As a result

$$\frac{|-\mathrm{d}p/\mathrm{d}x|}{\left|-\frac{\mathrm{d}p}{\mathrm{d}x}\right| + \left|\left(\frac{\rho_w - 1}{\rho}\right) \frac{1}{Fr} \left(\sin\beta \frac{\partial x}{\partial x_0} - \cos\beta \frac{\partial x}{\partial y_0}\right)\right|} \approx 0.8$$

when x is as small as 0.001.

3.2.3. *Solution near the leading edge*

In view of the above aspects of the flow and in order to circumvent problems arising near the forward stagnation point of the airfoil, we start integrating in the x-direction (see description of the numerical method in § 4) at a streamwise position x_s located near, but not exactly at, the leading edge. The details of the flow in the two phases at this point are obtained by solving the leading-order problem as $x \to 0$ assuming the usual flow structure near the forward stagnation point determined by pressure and shear forces,

$$\left.\begin{aligned} U &\approx Cx\frac{\mathrm{d}f_0}{\mathrm{d}\eta}, \quad C = 2L/\rho_L, \quad \eta = C^{1/2}(Y - \varepsilon H(x)), \\ u &\approx \frac{C^{1/2}}{H_0}x\frac{\partial F_0}{\partial z}, \quad z = \frac{y}{H(x)}, \quad H \approx H_0. \end{aligned}\right\} \tag{3.27}$$

In this fashion, functions f_0, F_0 and H_0 are obtained by the following set of equations:

$$\frac{\mathrm{d}f_0}{\mathrm{d}\eta} \to 1 \quad \text{as } \eta \to \infty, \tag{3.28}$$

$$\frac{\mathrm{d}^3 f_0}{\mathrm{d}\eta^3} - \left(\frac{\mathrm{d}f_0}{\mathrm{d}\eta}\right)^2 + f_0\frac{\mathrm{d}^2 f_0}{\mathrm{d}\eta^2} + 1 = 0, \tag{3.29}$$

$$\varepsilon^2\frac{\mu}{\mu_w}F(z=1) = f(\eta=0), \quad H_0 C\frac{\mathrm{d}f_0}{\mathrm{d}\eta}(\eta=0) = \frac{\mu}{\mu_w}\varepsilon\frac{\mathrm{d}F_0}{\mathrm{d}z}(z=1) \quad \text{at } \eta = 0, \quad z = 1, \tag{3.30}$$

$$H_0^2 C\frac{\mathrm{d}^2 f_0}{\mathrm{d}\eta^2}(\eta=0) = \frac{\mathrm{d}^2 F}{\mathrm{d}z^2}(z=1), \quad C^{1/2}F(z=1) = f_3(x_s), \quad H_0 = H(x_s), \tag{3.31}$$

$$CH_0F_0\frac{\mathrm{d}^2F_0}{\mathrm{d}\eta^2}\frac{\rho_w}{\rho}\left(\frac{\mu}{\mu_w}\right)^2\varepsilon^2 - \varepsilon^2\frac{\rho_w}{\rho}\left(\frac{\mu}{\mu_w}\right)^2 H_0 C\left(\frac{\mathrm{d}F_0}{\mathrm{d}z}\right)^2 + \frac{f_2(x_s)}{x_s} + \frac{C^{1/2}}{\varepsilon}\frac{\mathrm{d}F_0^3}{\mathrm{d}z^3} = 0, \tag{3.32}$$

$$F(z=0) = \frac{\mathrm{d}F_0}{\mathrm{d}z}(z=0) = 0, \tag{3.33}$$

given the starting location x_s and the parameter values; typically x_s is taken to be in the neighbourhood of 0.002. The effect of the particular location x_s on the initial flow properties enters the problem formulation through the values $f_3(x_s), f_2(x_s)$ that are used in the mass balance and x-momentum, respectively. Thus, equation (3.27) provides the initial condition for the integration along the airfoil surface. As it turns out, see also the next section, the evolution of the flow downstream does not depend on the location x_s, as long as this is restricted in the vicinity of the rounded leading edge, chosen as the starting point. This is an indication that the form of the solution as x increases constitutes a global attractor of the flow, in the context of the constant rainfall model that is used in the present study.

4. Numerical solution

The numerical solution of the governing equations, valid for any distance x, for flow past a curved surface, (2.7)–(2.17), or for flow past a flat plate, (3.2)–(3.10), is

obtained following the same approach that was used by Pelekasis & Acrivos (1995) in their study of forced convection and sedimentation of colloidal solid particles past a flat plate. More specifically, the transverse velocity in both phases is expressed in terms of the longitudinal one through an integral relation that arises upon application of continuity. This leaves only one unknown function to be calculated numerically in the gas stream, namely the longitudinal velocity which is obtained by solving the modified x-momentum equation, along with the location of the interface. In this fashion (2.8) becomes

$$U\frac{\partial U}{\partial x}+\left(\int_{\varepsilon H}^{Y}-\frac{\partial U}{\partial x}\mathrm{d}Y\right)\frac{\partial U}{\partial Y}+\varepsilon^2\frac{\mu}{\mu_w}\left(u\frac{\mathrm{d}H}{\mathrm{d}x}-f_3(x)\right)=-\frac{\mathrm{d}P}{\mathrm{d}x}+\frac{\partial^2 U}{\partial Y^2}, \tag{4.1}$$

where the interfacial mass balance (2.13) has been introduced in the above equation in order to replace the value of the transverse velocity at the interface. A similar equation is obtained for the film after application of continuity in (2.15):

$$\varepsilon^2\frac{\rho_w}{\rho}\left(\frac{\mu}{\mu_w}\right)^2\left(u\frac{\partial u}{\partial x}+\left(\int_0^{y}-\frac{\partial u}{\partial x}\mathrm{d}y\right)\frac{\partial u}{\partial y}\right)$$
$$=-\frac{\mathrm{d}p}{\mathrm{d}x}+\frac{1}{Fr}\left(\frac{\rho_w}{\rho}-1\right)\left(\sin\beta\frac{\partial x}{\partial x_0}-\cos\beta\frac{\partial x}{\partial y_0}\right)+\frac{1}{\varepsilon}\frac{\partial^2 u}{\partial y^2}. \tag{4.2}$$

The discretization of the x-momentum in both phases is described in the following and in most aspects it follows Pelekasis & Acrivos (1995).

Owing to the parabolic nature of the problem in the x-direction, time-like integration is performed in order to capture longitudinal variations of the unknown quantities via the second-order-accurate, $O(\Delta x^2)$, implicit trapezoidal rule. Owing to the very large longitudinal derivatives near the leading edge for flow past a flat plate, the integration starts at a streamwise location $x = x_I$ near the leading edge using the asymptotic result obtained as $x \to 0$. This does not affect the solution far from the leading edge, which indicates that the solution as $x \to \infty$ probably possesses similar properties, as an attractor, to the asymptotic solution presented by Nelson *et al.* (1995) assuming constant flow rate of the film. In the case of flow past a curved surface (in the present study the upper surface of a NACA-0008 airfoil was used) the flow near the leading edge is characterized by zero shear so there was no problem with initiating the time-like integration, as was the case with the flat plate for which shear becomes infinite at the leading edge. However, there was an issue of a different kind that had to be resolved, pertaining to the incorporation of the effect of gravity near the leading edge. More details on the numerical treatment of this issue are given at the end of this section.

In order to simplify the spatial discretization while working with a fixed mesh, we rewrite the governing equations in terms of $\bar{Y} = Y/H(x)$, $\bar{y} = y/H(x)$. In the case of an airfoil ε is not set to one and the chord length is used as the characteristic length scale in the x-direction. As a result ε is treated as an extra parameter of the problem. The resulting set of equations is discretized in the transverse direction via the Galerkin finite element method with the B-cubic splines as basis functions. Integration by parts eliminates second-order derivatives and increases the accuracy of the method to $O(h^3)$ where h is the size of the largest element. Special care is taken to verify the behaviour of the problem at infinity by doubling the length along the transverse direction that is discretized, and monitoring the value of the longitudinal velocity at the outer edge of the mesh so that it remains unchanged. Normally, a combination of 50 elements in the gas phase, 20 elements in the water film and a thousand steps in the x-direction was enough

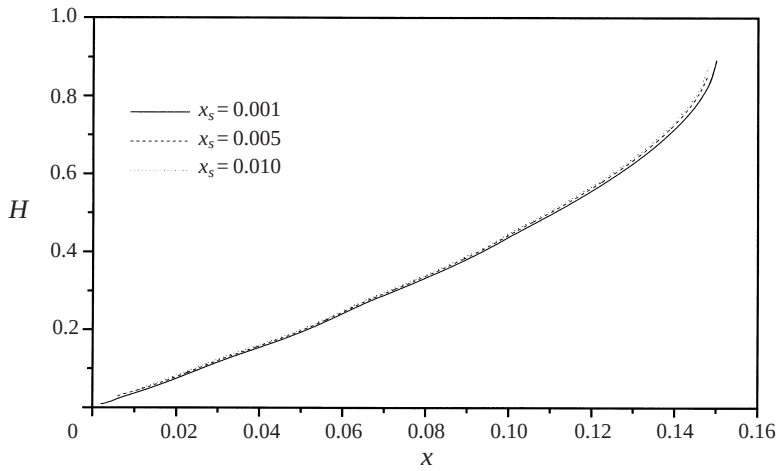

FIGURE 5. Evolution of the dimensionless film thickness, H, with varying location, x_0, on the airfoil surface where time integration starts; $\beta = -5°$, $Fr = 67$, $\varepsilon = 0.507$.

for the accurate description of the system within the third or second, at worst, significant digit. The procedure described above eventually gives rise to a set of nonlinear algebraic equations which is solved by Newton's iterations. More details on the problem reformulation in order to facilitate numerical solution, and on the finite element discretization via B-cubic splines in conjunction with time integration are given in Pelekasis & Acrivos (1995) and Pelekasis, Tsamopoulos & Manolis (1992), respectively.

The dependence of the downstream flow pattern at the location on the airfoil where time-like integration commences was investigated extensively. As was mentioned in the previous section, the flow quickly acquires its downstream structure irrespective of the starting location x_s. Figure 5 shows the evolution of the film thickness for three different starting locations x_s for the case with $Fr = 67$, $\beta = -5°$, $\varepsilon = 0.5$. The relatively wavy pattern in the evolution of the film thickness is due to the abrupt change in radius of curvature near the leading edge. The initial condition for each starting location was obtained via numerical solution of (3.28)–(3.33) using the methodology for the discretization in the transversal direction that was described above. 'Packing' of the elements near the interface in the gas phase was found to improve significantly the accuracy of results for certain parameter values. Owing to the nonlinear nature of the set of equations mentioned above multiple solutions were obtained. However only the one with positive longitudinal velocities in both phases was kept as it was the only one predicting physically meaningful velocity profiles.

Owing to the small value of Fr and the negative value of angle β, gravity counteracts pressure in the region between the leading edge and the position of maximum chord width, thus bringing about the early appearance of a Goldstein singularity. Nevertheless, the starting location of time-like integration in the x-direction does not affect the position where the singularity occurs, nor does it affect the downstream velocity profiles. In fact, it was found that the details of the initial velocity profile at x_s do not affect the downstream flow properties either, which also attests to the conjecture that the flow pattern obtained as x increases constitutes a global attractor of the flow.

The appearance of Goldstein singularities was a recurring theme in the present study. As will be seen in the next section they always appear at the airfoil wall and they are associated with vanishing shear stress, indicating flow reversal and eddy

Δx	Elements in the film	Elements in the gas	x_{sin}	H_{sin}	$\left(\frac{\partial u}{\partial z}\Big\|_{z=0}\right)_{sin}$
		$Fr = 67$			
10^{-3}	20	50	0.150	0.888	0.028
0.5×10^{-3}	20	50	0.1495	0.873	0.043
10^{-3}	40	50	0.150	0.888	0.028
10^{-3}	20	100	0.150	0.888	0.028
		$Fr = 269$			
10^{-3}	20	50	0.415	2.328	0.008
0.5×10^{-3}	20	50	0.4145	2.328	0.007
10^{-3}	40	50	0.414	2.328	0.008
10^{-3}	20	100	0.414	2.327	0.008
		$Fr = 1077$			
10^{-3}	20	50	0.534	3.019	0.013
0.5×10^{-3}	20	50	0.534	3.061	0.009
10^{-3}	40	50	0.534	3.019	0.013
10^{-3}	20	100	0.534	3.018	0.013

TABLE 1. Convergence tests for the location of the Goldstein singularity, for a NACA-0008 airfoil when $\beta = -5^\circ$ and $\varepsilon = 0.507$.

creation, and an abrupt increase in the film thickness. As was mentioned in the introduction they sometimes signify the onset of separation but not necessarily so. The current formulation that imposes pressure drop as it is specified in the outer layer cannot capture the flow region where eddies are formed, whether they arise due to flow separation or not, because in such regions longitudinal and transverse pressure drop are comparable in magnitude. This requires resorting to interactive formulation of the boundary layer so that pressure changes in the film are reflected in the gas stream. The proper context for such an approach is provided by the triple-deck formulation that captures the effect of disturbances in the flow field on the development of boundary layers, when the Reynolds number is sufficiently large (Tsao, Rothmayer & Ruban 1997; S. N. Timoshin & A. V. Vaganov 2000, private communication). In addition the simple marching numerical procedure adopted here has to be modified in order to capture flow recirculation. For the purposes of our study we will report the location where Goldstein singularities appear and use them as a measure of the *adversity* of flow of the two-fluid-system with varying parameter values. Table 1 gives the location of the singularity, x_{sin}, as well as the value of the film thickness and wall shear there when $\beta = -5^\circ$, $\varepsilon = 0.5$, for different levels of mesh refinement and for different values of Fr: $Fr = 67, 269, 1077$. The small value of the wall shear is evident as well as the accuracy of the computations (at least 3 significant digits for the location of the singularity)

5. Solution valid when $x \sim 1$

We are interested in obtaining velocity profiles at various downstream locations on the solid surface which can then be used as the basis for stability analysis.

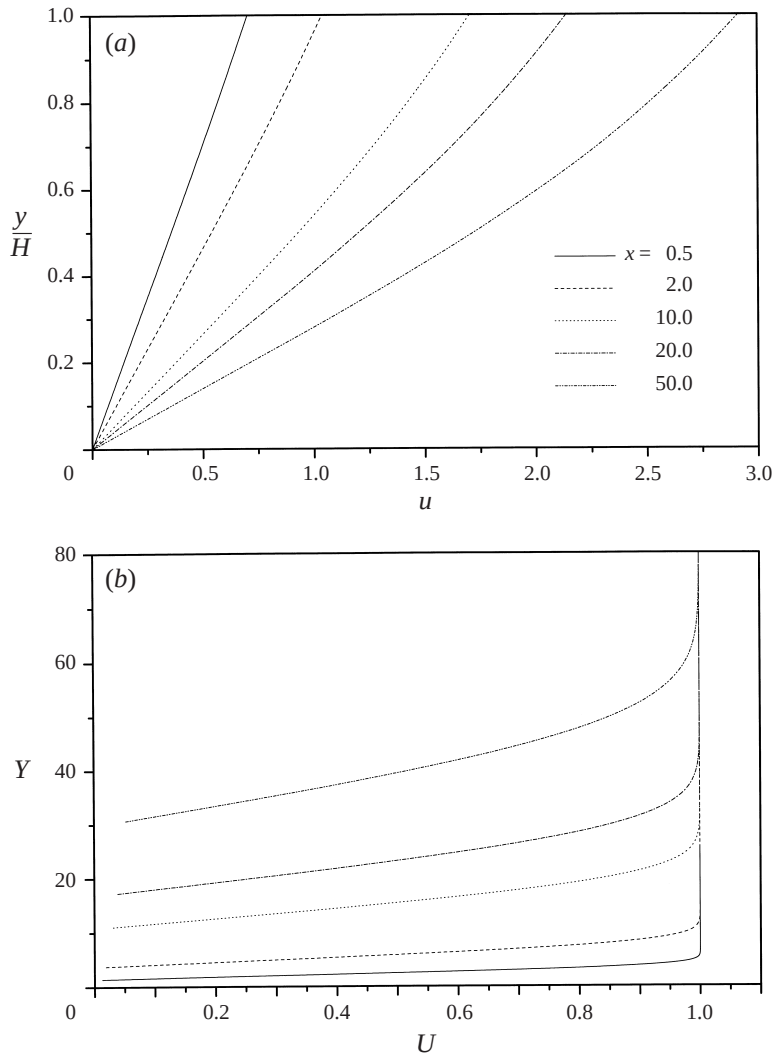

FIGURE 6. Evolution of the velocity profile with increasing distance from the leading edge, for flow past a flat plate, (*a*) in the film and (*b*) in the gas stream. The coordinates are scaled differently in each phase for convenience.

As the distance along the surface increases, asymptotic solutions obtained near the leading edge lose their validity and resorting to numerical solution, as described in the previous section, becomes unavoidable. A summary of the findings of the computational analysis is given in the following.

5.1. *Flow past a flat plate*

In this case it is the effect of inertia that builds up as the distance from the leading edge increases and this is reflected in the slower growth of the numerically predicted film thickness with x in comparison with the asymptotic solution, figure 2. Setting $\varepsilon = 1$ defines a new length scale, L^*, as was already explained in § 3.1, and leaves the ratio of densities and viscosities in the two phases as the only two problem parameters, along with the angle β which is set to zero in this case for simplicity. Thus, for the

air–water system, a single calculation is enough to provide us with all the necessary information for the behaviour of flow past a flat plate for different values of the rainfall rate, $\dot{r}$, the free-stream velocity, U_∞, and the plate length, L. Calculating L^* via $\varepsilon = 1$ and through it the ratio L/L^* we have the range of dimensionless values of x which are relevant to the particular set of flow parameters. As was pointed out before, for moderate values of $\dot{r}$ the asymptotic solution is more than enough for the description of the system. This is due partly to the small film thickness, $\varepsilon \ll 1$, but also to the small value of the quantity $(\rho_w/\rho)(\mu/\mu_w)^2$ for the air–water system, which determine the relative magnitude of film inertia. However, as $\dot{r}$ increases, larger values of dimensionless x become relevant and the asymptotic solution gradually loses validity. This can be seen from figure 2 but also from figures 6(a, b) where the evolution of the velocity profile is shown for the film and the gas stream, respectively, with increasing x. The gradual change from the linear profiles, corresponding to the simple shear conditions prevailing near the leading edge, to the parabolic-like profiles obtained at very large distances is evident and attests to the effect of inertia. The same pattern of linear axial velocity profile for most of the downstream region of the film flow has been reported by Beckett & Poots (1972) in their study of condensation heat transfer for planar geometry.

As was mentioned at the end of § 3.1 the similarity solution constitutes a valid approximation for a wide range of the relevant problem parameters for flow past a plate. Hence, the effect of rainfall and free-stream velocity on film growth can be demonstrated by focusing on the effect that they have on the leading-order asymptotic prediction for the dimensional film thickness obtained from (3.1),

$$H' = H_f \left(\frac{x'}{L^*}\right)^{3/4} \frac{2}{\sqrt{0.332}}. \tag{5.1}$$

Upon close examination of the ratio $(H_f/L^*)^{3/4}$, along with (2.20), it is seen that the dimensional film thickness, H', is inversely proportional to the 3/4 power of the free-stream velocity, U_∞, thus reflecting the effect of shear imposed from the boundary layer on the film growth. On the other hand the effect of rainfall is to increase the dimensional film thickness with the 1/2 power of the rainfall rate $\dot{r}$. However, for very large rainfall rates the flow is described by the full equations, $x \sim 1$, in most of the plate. Then the growth rate of the film will be reduced by inertia, as was shown in figure 2, and the effect on the dimensional thickness is not as obvious. Figure 7 shows the evolution of H' with the distance from the leading edge, x', for flow past a flat plate with length, $L = 1$ m, of an air stream with free-stream velocity $U_\infty = 60\,\mathrm{m\,s^{-1}}$ and for a wide range of values of the rainfall rate, $\dot{r} = 45, 180,$ and $360\,\mathrm{mm\,h^{-1}}$. The trend of increasing film thickness with the square-root of the rainfall rate is evident for the entire range of values of the latter quantity, as shown in figure 7.

5.2. *Flow past the upper surface of a NACA-0008 airfoil*

The effect of curvature on the flow pattern that is established above a solid surface is investigated numerically using a NACA-0008 airfoil. Its exact shape, as well as its aerodynamic properties are given in the literature (Abbott & Doenhoff 1949). First, the effect of increased film thickness is investigated through the increase of parameter ε. As can be seen from figure 8(a), the growth rate of the film is not significantly affected by the change in ε, except for the downstream region. This can be explained in view of the asymptotic solution in the limit as $\varepsilon \to 0$, (3.24), and more specifically by equation (3.26) which gives an estimate for the first-order correction in ε for the

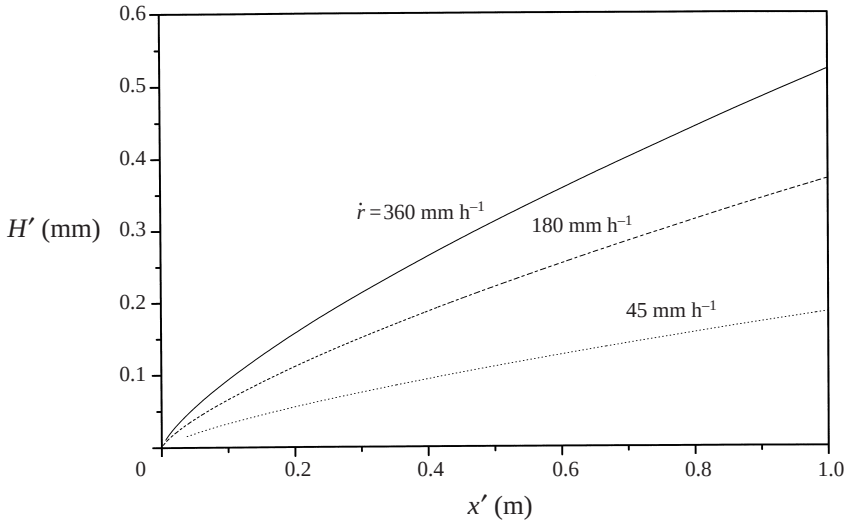

FIGURE 7. Evolution of the dimensional film thickness for flow past a flat plate and for increasing rainfall rate; $U_\infty = 60\,\mathrm{m\,s^{-1}}$, $\beta = 0°$.

evolution of the film thickness, that accounts for the effect of pressure drop in the film. The latter acquires very large values in a thin region near the leading edge, figure 4(*b*). Nevertheless it does not significantly affect the film growth rate, even as ε increases, because the dimensionless film thickness, H, is very small in the same region. In the region beyond the position of maximum airfoil thickness, the deceleration region, the pressure drop quickly becomes significantly smaller, thus explaining the weak effect of ε on the film growth rate. It can also be seen easily by examining (3.26) that increasing ε results in a slight increase of the film thickness in the deceleration region of the airfoil, where the pressure drop acquires small positive values, which is in agreement with the numerical prediction for the evolution of the film thickness shown in figure 8(*a*). Of course, equations (3.24) and (3.26) have limited validity in the downstream region where the effect of the adverse pressure gradient becomes important and the film thickness increases abruptly as the flow seems to approach, without actually reaching, a Goldstein singularity, figure 8(*a*). However, the total effect of increasing ε, e.g. through $\dot{r}$, is to significantly increase the dimensional film thickness, $H' = H_f H$ (figure 8*b*), basically through H_f which grows like $\dot{r}^{1/2}$.

Another important effect of increasing ε can be gleaned from figure 9(*a*, *b*) where the film thickness evolution is given for a wide range of rainfall rates, $22.5 < \dot{r} < 5760\,\mathrm{mm\,h^{-1}}$, but for smaller chord length, $L = 0.3\,\mathrm{m}$ vs. 1 m, and free-stream velocity, $U_\infty = 50\,\mathrm{m\,s^{-1}}$ vs. $60\,\mathrm{m\,s^{-1}}$, compared to figures 7 and 8(*a*, *b*), so that Fr is now 855 rather than 360. Again, as in figure 8(*a*, *b*), the dimensionless film thickness is increasing slightly with increasing ε while the dimensional one is increasing like $\dot{r}^{1/2}$. Nevertheless, in the case of larger Fr, figure 9(*a*, *b*) reveals a stronger tendency of the flow to exhibit Goldstein singularities in the downstream region of the airfoil. This can also be seen in figures 10(*a*, *b*) and 11(*a*, *b*) where the evolution of the velocity profile inside and outside the film is shown at different downstream locations when the flow evolves until far downstream (figure 10*a*, *b*) and when the flow exhibits a Goldstein singularity early in the downstream region (figure 11*a*, *b*). In the former case, despite the fact that the flow remains 'regular', the effect of the adverse pressure gradient is evident in the velocity profile in the liquid film, figure 10(*a*), through the

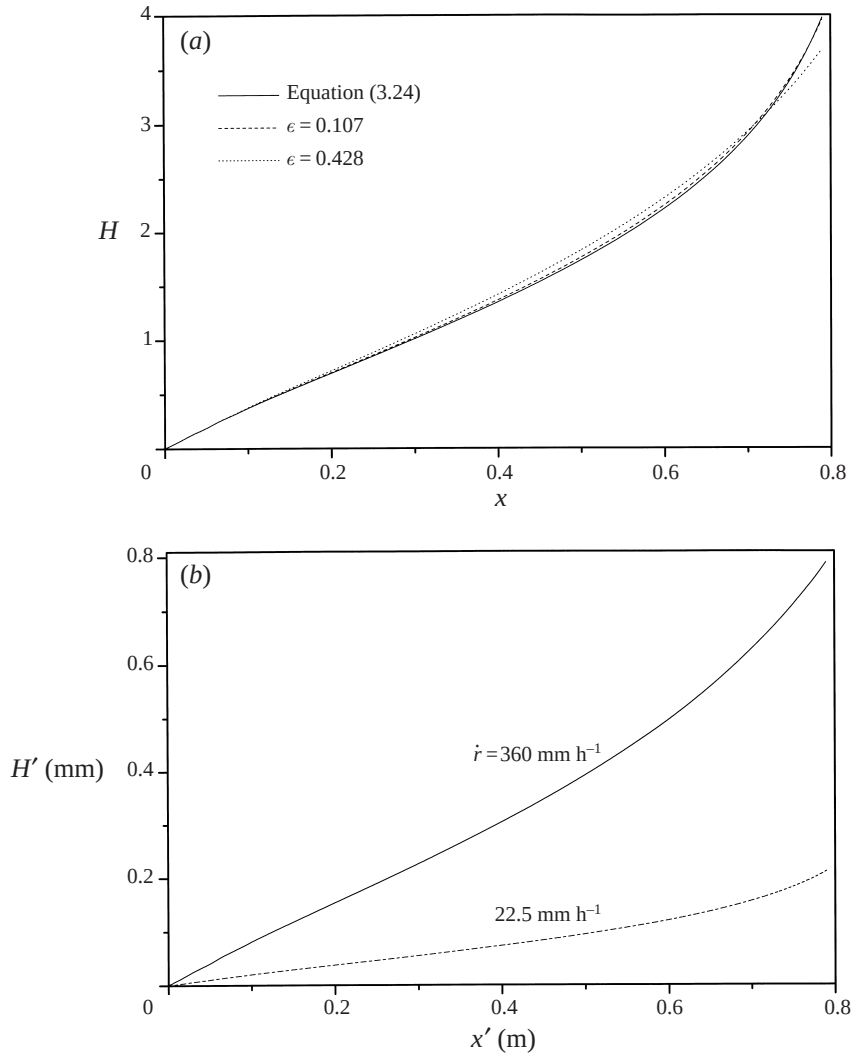

FIGURE 8. Evolution of (a) the dimensionless film thickness for flow past a NACA-0008 airfoil, as predicted by the asymptotic solution as $\varepsilon \to 0$, equation (3.24), and for increasing values of $\varepsilon = 0.107, 0.428$ ($\beta^\circ = 0, Fr = 369$); ($b$) the dimensional film thickness with increasing rainfall rate ($L = 1.0\,\mathrm{m}$, $U_\infty = 60\,\mathrm{m\,s^{-1}}$, $\dot{r} = 22.5\,\mathrm{mm\,h^{-1}}$, when $\varepsilon = 0.107$, $\dot{r} = 360\,\mathrm{mm\,h^{-1}}$ when $\varepsilon = 0.428$).

reduction in shear at the solid surface and the appearance of an inflection point in the velocity profile in the gas stream, figure 10(b). On the other hand, the vanishing velocity gradient at the wall in the liquid film can be clearly seen in figure 11(a) near $x = 0.7$. The reason for this phenomenon is the adverse pressure gradient that the flow encounters in the downstream region of the flow, that is imposed on it by the far field. This adverse pressure gradient opposes downstream film flow, hence the steep rise of the film thickness near the point where the singularity arises in figure 9(a, b). The same type of film growth was observed near the point of singularity by Beckett & Poots (1972) in their study of boundary layer flow past a cylinder in the presence of film condensation. When $Fr = 360$ gravitational forces play an important role counteracting pressure forces, since the angle of attack β is positive and the pressure

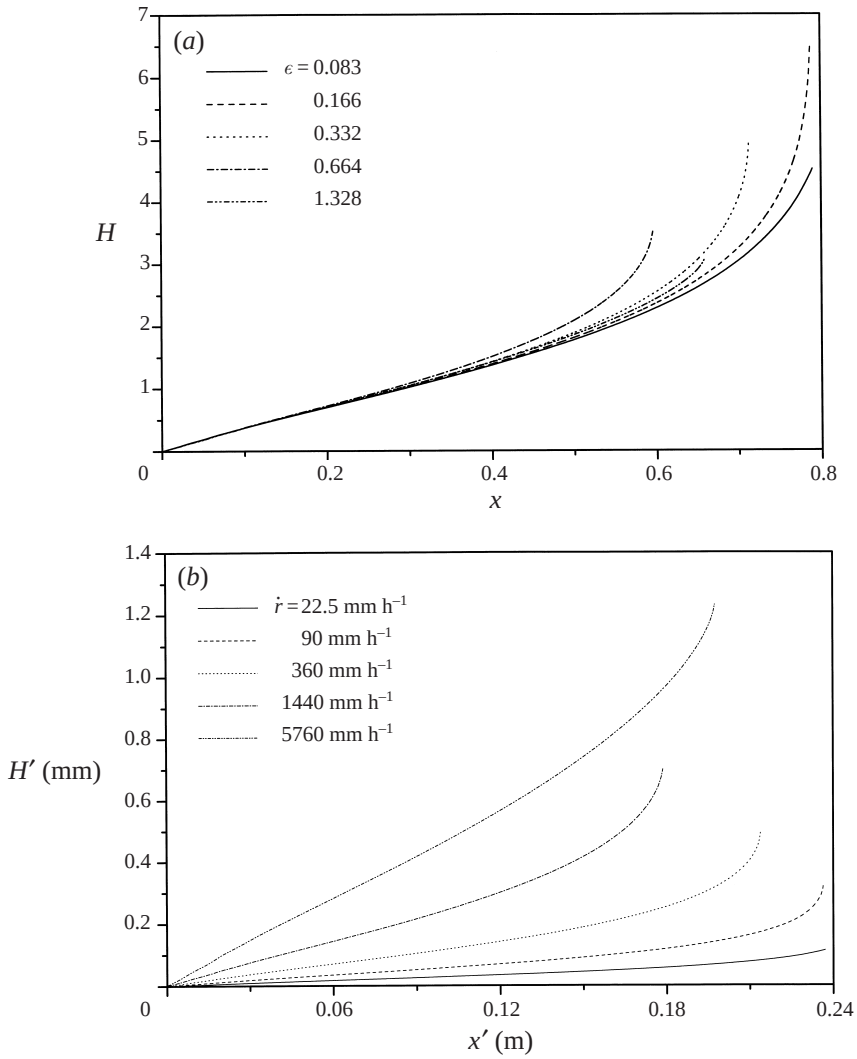

FIGURE 9. Evolution of (*a*) the dimensionless film thickness for flow past a NACA-0008 airfoil, with increasing values of ε; (*b*) the dimensional film thickness with the equivalent increasing values of the rainfall rate $\dot{r}$ ($L = 0.3$ m, $U_\infty = 50$ m s^{-1}, $\beta^\circ = 0$, $Fr = 885$).

drop is significantly reduced in magnitude far from the leading edge of the airfoil, thus postponing the advent of singularity. As Fr increases, the effect of gravity is decreased and the appearance of singularities becomes possible.

It should be noted that inflection points appear in the velocity profile in the gas stream in figure 11(*b*) as well. Moreover they appear before the appearance of singularities, indicating that eddy formation as a dynamic effect might anticipate the effect of singularities in the two-fluid system (Bhaskaran & Rothmayer 1998). Computations cannot proceed beyond this point because, as was mentioned in the previous section, the longitudinal pressure drop in the bulk of the gas stream is affected by pressure changes in the boundary layer as well as the liquid film. Thus, interactive boundary layer formulation or condensed boundary layer formulation becomes indispensable, either in the context of triple-deck theory (S. N. Timoshin

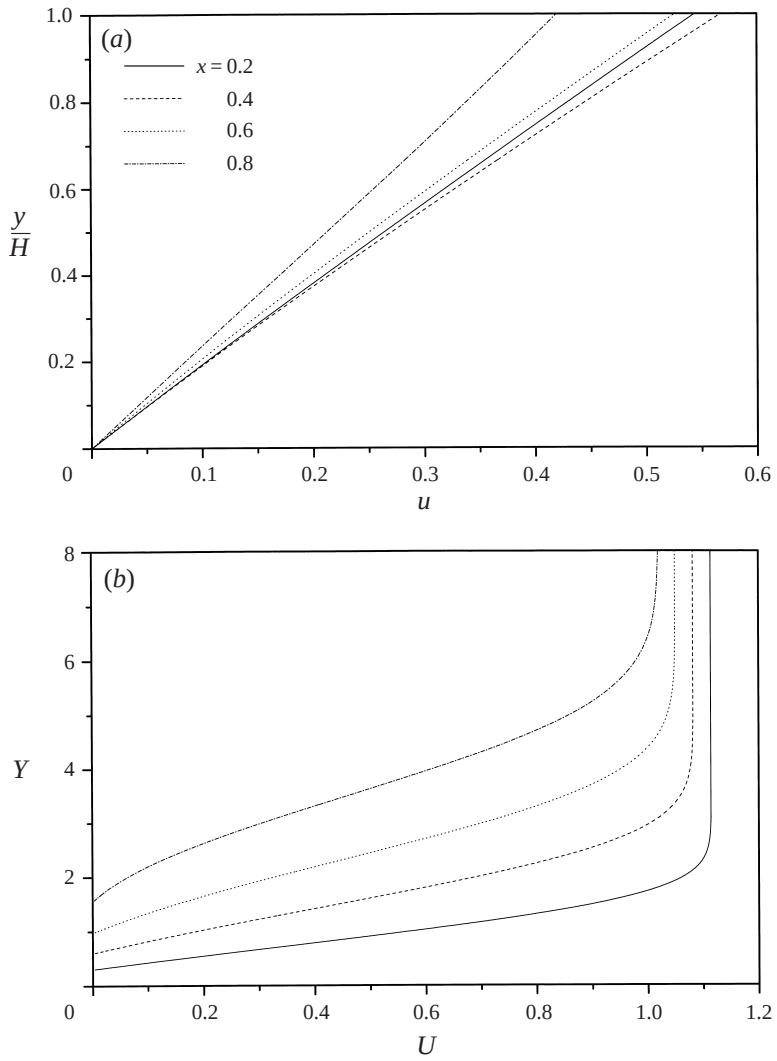

FIGURE 10. Evolution of the velocity profile with increasing distance from the leading edge, for flow past a NACA-0008 airfoil, (*a*) in the film and (*b*) in the gas stream; $L = 1.0\,\mathrm{m}$, $U_\infty = 60\,\mathrm{m\,s^{-1}}$, $\dot{r} = 360\,\mathrm{mm\,h^{-1}}$, $\beta^\circ = 0$, $Fr = 369$. The coordinates are scaled differently in each phase for convenience.

& A. V. Vaganov 2000, personal communication), or via strong coupling numerical methods (Fletcher 1988).

It should be noted also that as ε increases, while still remaining relatively small $\varepsilon < 0.6$, the point of singularity is transferred upstream. This seems to negate the expected lubricating effect of water on the flow of air. However, this should be anticipated since in the limit as $\varepsilon \to 0$ inertia drops out of (2.15) and the lubricating properties of water – high density and low viscosity – play no role in the solution. Then, as ε increases, the effect of pressure drop, which basically balances viscous shear, is intensified resulting in larger positive values of the second derivative, $\partial^2 u/\partial y^2$, near the surface. This, combined with the fact that the second derivative is expected to be negative at the outer edge of the boundary layer in the gas phase, leads to the

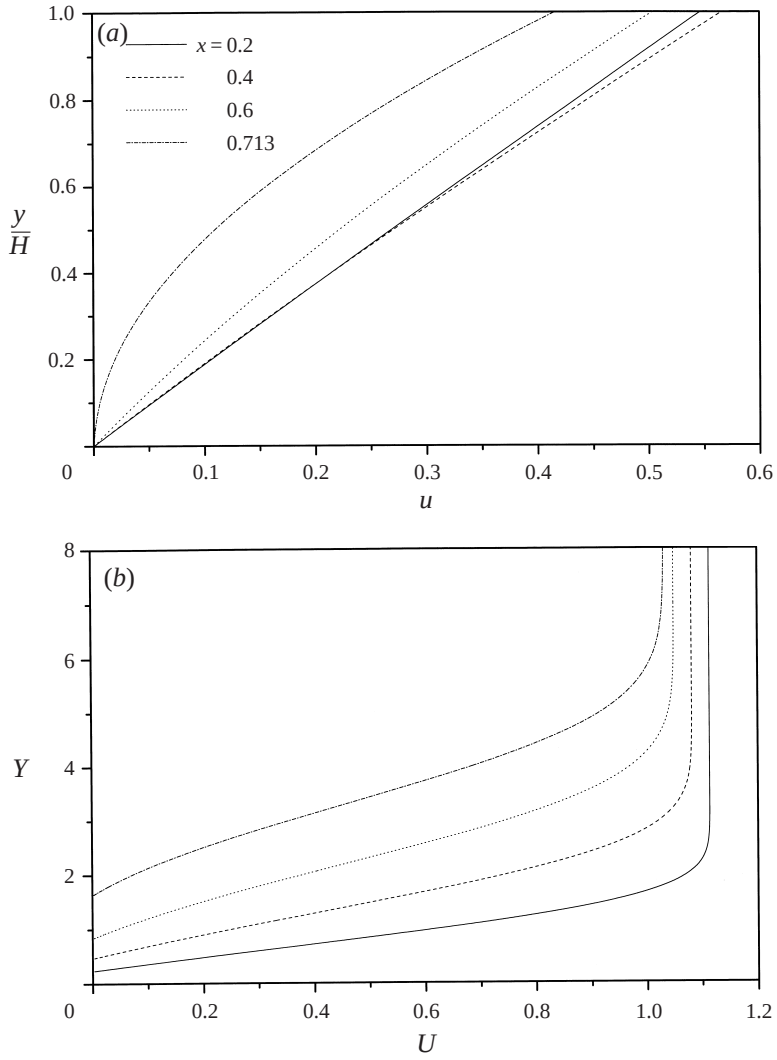

FIGURE 11. As figure 10 but for $L = 0.3\,\mathrm{m}$, $U_\infty = 50\,\mathrm{m\,s^{-1}}$, $Fr = 885$.

conclusion that an inflection point will appear in the velocity profile. In fact, it will first occur near the airfoil surface and its occurrence is accelerated with further increasing values of ε. This pattern persists as long as ε does not grow significantly, in which case inertia becomes important, generating a lubricating effect and moving the singularity downstream: the curve corresponding to $\varepsilon = 1.328$ in figure 9(a) with $\dot{r} = 360\,\mathrm{mm\,h^{-1}}$. Therefore, a critical film thickness exists beyond which water has a lubricating effect on the gas stream.

The effect of gravity in the flow of the water film is incorporated in the Froude number, Fr. When angle β is positive, referring to a take-off situation, gravity assists the flow of the film towards the downstream region where an adverse pressure gradient exists. As Fr decreases the beneficial effect of gravity is evident in the delay of the appearance of the singularity, figure 12. On the other hand, when angle β is negative, referring to a landing situation, gravity acts in the opposite direction to the main flow resulting in an early appearance of the singularity, sometimes even before the position

$L = 0.3\,\text{m}$, $U_\infty = 50\,\text{m s}^{-1}$, $Fr = 885$, $\beta = 0^\circ$

ε	x_{sin}
0.083	—
0.0166	0.788
0.332	0.713
0.664	0.596
1.328	0.659

ε	Fr	$\beta(deg.)$	x_{sin}
0.664	428	+5	—
0.664	1710	+5	0.662
0.507	67	−5	0.150
0.507	269	−5	0.415
0.507	1077	−5	0.534
0.545	606	+5	—
0.545	606	0	0.712
0.545	606	−5	0.490

TABLE 2. Location of the Goldstein singularity with varying parameters of the problem.

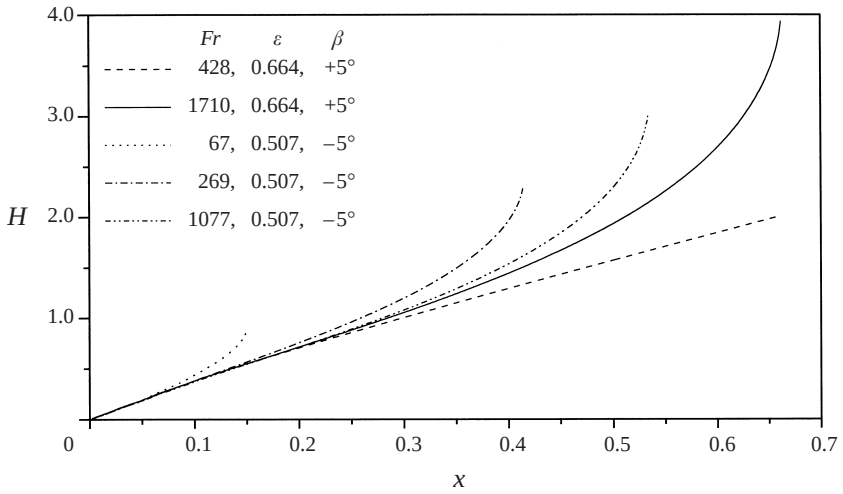

FIGURE 12. Evolution of the dimensionless film thickness with increasing distance from the leading edge and varying Fr for positive ($\beta = 5^\circ$, $\varepsilon = 0.664$) and negative ($\beta = -5^\circ$, $\varepsilon = 0.507$) angles.

of maximum chord width is reached. In this case increasing Fr decelerates the advent of singularity, figure 12. In general, negative angles produce an unfavourable situation for the film flow, enhancing the appearance of singularities and consequently flow reversal, whereas positive angles act in such a way as to sustain continuous film flow. It should also be noted that in the latter case, $\beta \geqslant 0$, decreasing Fr results in reduction of the critical value of ε, or equivalently reduces the critical rainfall rate beyond which the water film actually acts as a lubricant, postponing flow reversal and the formation of eddies. The location of singularities for the cases shown in figure 9(a, b) and in figure 12 as well as those obtained by varying Fr and β are shown in table 2.

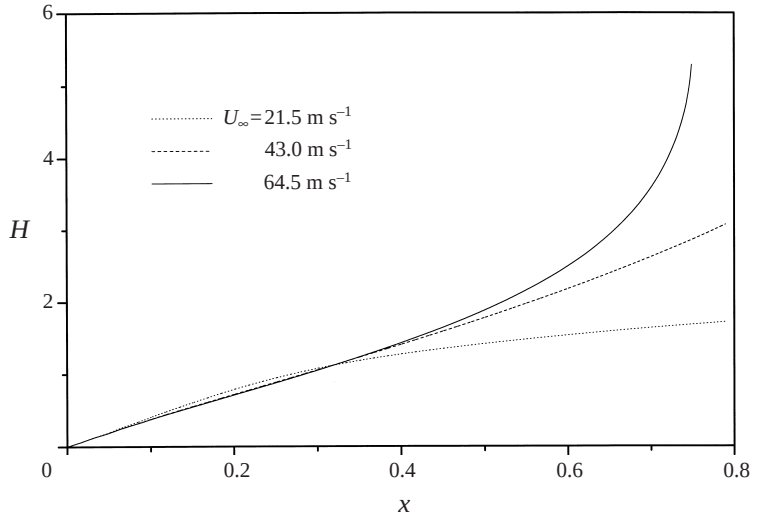

FIGURE 13. Evolution of the dimensionless film thickness with increasing U_∞; $\beta = 0°$, $L = 0.7$ m, $\dot{r} = 360\,\mathrm{mm\,h^{-1}}$.

As was seen in § 5.1 for flow past a flat plate, the constant-rainfall-rate model presented here predicts an increasing film thickness with increasing rainfall rate, $\dot{r}$, and decreasing free-stream velocity, U_∞. The same trend was found to exist in the case of a curved surface, i.e. NACA-0008 airfoil. The effect of rainfall was discussed extensively in § 5.2 and is depicted in figures 8 and 9. The effect of varying free-stream velocity is twofold since it affects both Fr and ε. As U_∞ increases Fr increases as well, which results in the attenuation of the effect of gravity and the accompanying deceleration or acceleration in the appearance of singularities depending on the sign of β. At the same time ε is reduced, thus leading to slightly smaller dimensionless film thickness. Figure 13 depicts this type of behaviour in the evolution of the dimensionless film thickness with increasing U_∞ and for typical values of the rest of the parameters: $\dot{r} = 360\,\mathrm{mm\,h^{-1}}$, $L = 70\,\mathrm{cm}$, $\beta = 0°$. The appearance of singularities with increasing U_∞ is also evident. It should be noted, however, that the net effect of increasing U_∞ is a significant reduction in the dimensional film thickness, far from the region near the singular point, due to the more pronounced reduction in H_f, $H_f \approx U_\infty^{-3/4}$.

Clearly, the two geometries that were investigated exhibit qualitative similarities as regards the evolution and growth of the water film. This is, partly, attributed to the fact that the shape of the NACA-0008 airfoil does not differ significantly from that of a flat plate due to its relatively small maximum thickness, 8% of the chord length. A major difference between the two flow situations lies in the airfoil curvature, which generates adverse pressure gradients in the downstream region of the airfoil. Such pressure gradients are known to cause flow separation. However, this does not happen as often as one might expect because gravity, especially when the angle $\beta \geqslant 0$, counteracts pressure and allows continuous film flow. Figure 14 compares the dimensional film thickness, H', as a function of x' for a representative set of parameter values, $U_\infty = 35\,\mathrm{m\,s^{-1}}$, $\dot{r} = 360\,\mathrm{mm\,h^{-1}}$, $L = 0.7\,\mathrm{m}$, $\beta = 0$, with x' denoting distance along the plate and the airfoil upper surface. As can be seen from the two curves in figure 14 the predicted film thickness is similar in order of magnitude with

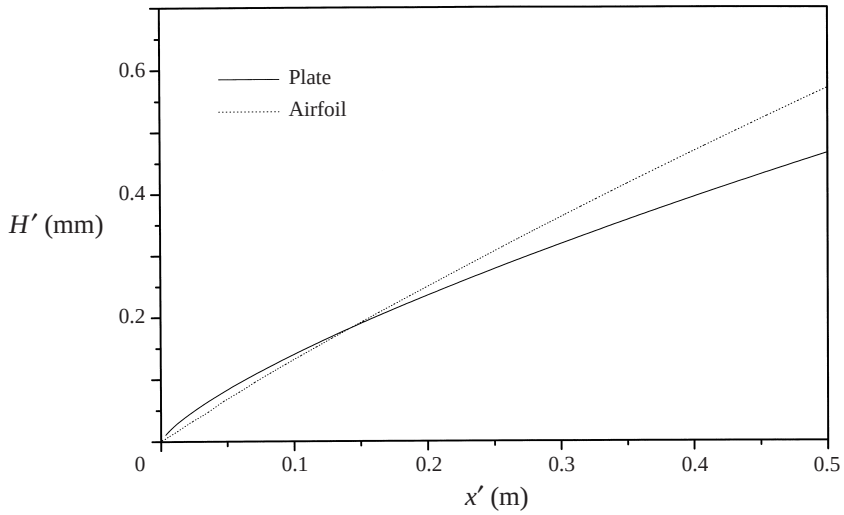

FIGURE 14. Evolution of the dimensionless film thickness as predicted for flow past a flat plate and for flow past a NACA-0008 airfoil; $L = 0.7\,\mathrm{m}$, $U_\infty = 35\,\mathrm{m\,s^{-1}}$, $\beta = 0°$, $\dot{r} = 360\,\mathrm{mm\,h^{-1}}$.

the difference that, near the leading edge, the airfoil exhibits a slower growth rate due to its more rounded shape that does not capture raindrops as efficiently, and in the downstream area adverse pressure gradients lead to increased film thickness on the airfoil surface. The latter effect becomes more pronounced as U_∞ increases, in which case the adverse pressure gradients in the downstream region are large enough to produce Goldstein-type singularities.

Such discrepancies, however, are not particularly important since the region where most of the interesting dynamic phenomena evolve is before the $x'/c = 0.6$ location and after the rounded region near the leading edge. Indeed this has been observed by various researchers who conducted experiments with test wing sections in wind tunnels under conditions that simulate rainfall. As was mentioned in the introduction, Feo & Gonzalez (1988) and Hastings & Manuel (1985), among others, measured film thickness characteristics in the wind tunnel facility at NASA-Langley, and they captured the increase in film thickness with increasing rainfall rate, or equivalently with increasing liquid water content in the air stream, and decreasing free-stream velocity, or with decreasing Reynolds number in the gas stream. In addition, they observed the formation of longitudinal waves in the region $0.1 \leqslant x'/c \leqslant 0.5$ of a NACA 64-210 airfoil followed by three-dimensional rivulets. Thus, they attributed the reduced aerodynamic performance of the airfoil under rainfall conditions to premature boundary layer separation.

6. Conclusion

Upon comparison of the results shown here with those obtained via experimental investigations we can conclude that the general trends in the film behaviour as a function of the rainfall rate and the free-stream velocity have been captured. The maximum film thickness that was measured for similar values of the control variables, even though it is in general larger than the one predicted here, is of the same order of magnitude (0.5 mm). In addition, the conjecture of premature boundary layer separation seems to be corroborated by the findings of the present study, to the extent

that the singularities appearing on the airfoil wall can be associated with separation. Nevertheless, there is every indication that the film presence can cause early flow reversal and eddy creation (figure 9*a*, *b*), which is probably due to separation and will, in any case, disturb the flow of the gas stream. Further research is required in order to verify the connection between the appearance of singularities and separation, and emphasis has to be placed on an interactive boundary layer formulation, (Tsao *et al*. 1997); S. N. Timoshin & A. V. Vaganov (2000, personal communication). Of course, this is all in the context of steady-state calculations. The evolution of the film thickness occurs in a different fashion. This is a result of the wavy nature of the interface which cannot be captured by the present study since it is an inherently dynamic phenomenon. What has been captured is a reliable and almost quantitatively correct steady state that can be used as a basis for our stability analysis. In fact, for a wide range of parameter values the flat-plate geometry provides a reliable and tractable starting point for examining the dynamic behaviour of boundary layer flow in the presence of rainfall.

As was pointed out in the previous section, inflection points appear in the velocity profile in the gas stream before the appearance of singularities or even when singularities do not appear at all, (figures 10*b*, 11*b*). This is an indication that a Rayleigh type of instability may arise that can also produce eddies before boundary layer separation takes place (Bhaskaran & Rothmayer 1998). Another dynamic effect that has also to be accounted for is the appearance of Tollmien–Schlichting waves, which are generated in the bulk of the gas stream, and interfacial waves which arise as a result of the dynamic interaction between the film free surface and the boundary layer. Such a task has already been undertaken by Pelekasis & Tsamopoulos (2001), for the planar flow configuration obtained neglecting film inertia in the limit as $x \to 0$, with interesting findings on the importance of interfacial waves in boundary layer stability.

The authors wish to acknowledge financial support by the University of Patras Research Foundation through the 'Caratheothory' research program.

REFERENCES

Abbott, I. A. & Doenhoff, A. E. von 1949 *Theory of Wing Sections*, pp. 111–115, 312. McGraw-Hill.

Acrivos, A. & Herbolzheimer, E. 1979 Enhanced sedimentation in settling tanks with inclined walls. *J. Fluid Mech.* **92**, 435–457.

Beckett, P. & Poots, G. 1972 Laminar flow condensation in forced flows. *Q. J. Mech. Appl. Maths* **25**, 125–152.

Bender, C. M. & Orszag, S. A. 1978 *Advanced Mathematical Methods for Scientists and Engineers*. McGraw-Hill.

Benjamin, T. B. 1958 Shearing flow over a wavy boundary. *J. Fluid Mech.* **6**, 161–205.

Bezos, M. G., Dunham, R. E. Gentry, L. G. & Melson, W. E. 1992 Wind tunnel aerodynamic characteristics of a transport-type airfoil in a simulated heavy rain environment. *NASA TP* 3184.

Bhaskaran, R. & Rothmayer, A. P. 1998 Separation and instabilities in the viscous flow over airfoil leading edges. *Computers Fluids* **27**, 903–921.

Cambell, B. A. & Bezos, M. 1989 Steady-state and transitional aerodynamic characteristics of a wing in simulated heavy rain. *NASA TP*-2932.

Dunham, R. E. Jr 1987 The potential influence of rain on airfoil performance. Lecture presented at the Von Karman Institute for Fluid Dynamics, Belgium.

Feo, A. & Gonzalez, P. 1988 Water film thickness measurements on an airfoil surface in a water-spray from NASA-Langley's 4 × 7 meter wind tunnel tests. *INTA* N/221/510/89.004.

Fletcher, C. A. J. 1988 *Computational Techniques for Fluid Dynamics*, Vol. II, Section 16.3.4. Springer.

GOLDSTEIN, S. 1948 On laminar boundary-layer flow near a position of separation. *Q. J. Mech.* **1**, 43–69.

HASTINGS, E. C. & MANUEL, G. S. 1985 Measurements of water film characteristics on airfoil surface from wind tunnel tests with simulated heavy rain. *AIAA Paper* 85-0259.

HOOPER, A. P. & BOYD, W. G. C. 1987 Shear-flow instability due to a wall and a viscosity discontinuity at the interface. *J. Fluid Mech.* **179**, 201–225.

NELSON, J. J., ALVING, A. E. & JOSEPH, D. D. 1995 Boundary layer flow of air over water on a flat plate. *J. Fluid Mech.* **284**, 159–169.

OZGEN, S., DEGREZ, G. & SARMA, G. S. R. 1998 Two-fluid boundary layer stability. *Phys. Fluids* **10**, 2746–2757.

PELEKASIS, N. A. & ACRIVOS, A. 1995 Forced convection and sedimentation past a flat plate. *J. Fluid Mech.* **294**, 301–321.

PELEKASIS, N. A. & TSAMOPOULOS, J. A. 2001 Linear stability of a gas boundary layer flowing past a thin liquid film over a flat plate. *J. Fluid Mech.* (to appear).

PELEKASIS, N. A., TSAMOPOULOS, J. A. & MANOLIS, G. D. 1992 A hybrid finite-boundary element method for inviscid flows with free surface. *J. Comput. Phys.* **254**, 501–527.

ROSENHEAD, L. (Ed.) 1963 *Laminar Boundary Layers*, pp. 201–203, 231–232, 260–261. Clarendon.

SHAQFEH, E. S. G. & ACRIVOS, A. 1986 The effects of inertia on the buoyancy-driven convection flow in settling vessels having inclined walls. *Phys. Fluids* **29**, 3935–3948.

SHAQFEH, E. S. G. & ACRIVOS, A. 1987 The effects of inertia on the stability of the convective flow in inclined particle settlers. *Phys. Fluids* **30**, 960–973.

SHU, J.-J. & WILKS, G. 1995 Mixed-convection laminar film condensation on a semi-infinite vertical plate. *J. Fluid Mech.* **300**, 207–229.

THOMSON, B. E., JANG, J. & DION, J. L. 1995 Wing performance in moderate rain. *J. Aircraft* **24**, 1034–1039.

THWAITES, B. (Ed.) 1960 *Incompressible Aerodynamics*, pp. 113–130. Clarendon.

TIMOSHIN, S. N. 1997 Instabilities in a high-Reynolds-number boundary layer on a film-coated surface. *J. Fluid Mech.* **353**, 163–195.

TSAO, J-C., ROTHMAYER, A. P. & RUBAN, A. I. 1997 Stability of air flow past thin liquid films on airfoils. *Computers Fluids* **26**, 427–452.

YIH, C.-S. 1990 Wave formation on a liquid layer for de-icing airplane wings. *J. Fluid Mech.* **212**, 41–53.